Porous ceramic solid electrolyte for Na+ ion batteries.

Auteur : Roni, Md Rafiul Alam
Promoteur(s) : Job, Nathalie
Faculté : Faculté des Sciences appliquées
Diplôme : Master : ingénieur civil en chimie et science des matériaux, à finalité spécialisée en Advanced Materials - Innovative Recycling
Année académique : 2023-2024
URI/URL : http://hdl.handle.net/2268.2/20465

UNIVERSITY OF LIEGE
FACULTY OF APPLIED SCIENCE

DEVELOPMENT OF POROUS SOLID CERAMIC ELECTROLYTE SCAFFOLD FOR SODIUM ION BATTERIES

Md Rafiul Alam RONI

Thesis presented for obtaining the master's degree in Chemical and Materials engineering

Supervisor:
Prof. Nathalie Job

!! The data included in this thesis are confidential. The supervisor must give his consent before consultation!!

Abstract

Owing to growing energy demand, awareness of the critical elements and the safety issues originating from liquid electrolytes, research in sodium all-solid-state batteries (SIBs) are gaining significant attention. However, the advancement is being challenged due to lower electrolyte/electrode interfacial contact and longer ion migration pathway. Recent studies showed the viability of producing porous multilayer ceramic electrolyte structure and infiltrating the active materials into it. Despite multifaceted approach, maintaining uniform surface contact still has been a challenge due to incomplete loading of active materials. This incomplete loading is a consequence of the disorientation and tortuosity of the pores formed during the fabrication process of the ceramic. Our research addressed this issue and successfully developed unidirectionally oriented porous scaffold of NASICON-type $Na_{3.4}Zr_2Si_{2.4}P_{0.6}O_{12}$ (NZSP) ceramic electrolyte, replicating the microstructure of wood. Two different types of woods, namely balsa and american western red cedar were pyrolyzed and infiltrated with NZSP ceramic slurry. After sintering, the pore diameter was 5 – 15 µm, and the void fraction was 40% – 45%. This novel architecture promises the possibility to facilitate complete loading of active materials and significantly reduce the ion migration pathway.

Table of contents

1 Introduction 6

1.1 Background and significance 6
1.2 Na-ion batteries: an alternative to Li-ion batteries 6
1.3 Na-ion batteries: working principle and architectures 7
1.4 Choice of solid-state electrolytes (SSEs) for Na-ion batteries 8
1.5 NASICON-type electrolytes 10
1.6 Current state of the art 11
1.7 Objective of the thesis 14

2 Methodology 15

2.1 Theoretical and experimental background 15
2.2 Selection of wood templates 16
2.3 Materials characterization methods 17
2.3.1 Scanning electron microscopy (SEM) 17
2.3.2 X-ray diffraction (XRD) 18
2.3.3 ThermoGravimetric Analysis (TGA) 19

3 Experimental procedure 20

3.1 Materials, chemicals and reagents 20
3.2 Steps of experiment 20
3.2.1 Carbon template preparation 20
3.2.2 Infiltration 21
3.2.3 Sintering 22
3.3 Sintering support preparation 23
3.4 Materials characterization 23

4 Results and discussion 24

4.1 Carbon template preparation 24
4.1.1 Unravelling the microstructure of wood 24
4.1.2 Chemical treatment 25
4.1.3 ThermoGravimetric Analysis (TGA) 26
4.1.4 Microstructure analysis of pyrolyzed wood 28

4.1.5 Thermal behavior of wood during pyrolysis....30
4.2 NZSP powder processing and infiltration into carbon template....33
4.2.1 NZSP powder processing....33
4.2.2 Infiltration of NZSP into carbon template....35
4.3 Sintering studies of NZSP ceramic....38
4.3.1 Analysis of sintered ceramic based on infiltration method....38
4.3.2 Ceramic with optimized slurry and cyclic infiltration....41
4.3.3 Thermal studies of the sintered ceramic....44
5 EIT chapter....46
5.1 Life cycle and circular economy....46
5.2 Techno-economic Analysis....48
5.2.1 Technological analysis....48
5.2.2 Economic Analysis....49
5.3 SWOT analysis....51
5.3.1 Strength....51
5.3.2 Weakness....51
5.3.3 Opportunities....52
5.3.4 Strength....52
6 Conclusion and future direction....53
6.1 Conclusion....53
6.2 Future direction....53
7 References....56

1 Introduction

1.1 Background and significance

With the increasing use of portable devices, electric vehicles (EVs), and shift to renewable energy sources to mitigate environmental issues arising from fossil fuel-based energy sources, the demand for efficient and sustainable energy storage systems increased as well. Since their introduction in the 1990s, of lithium-ion batteries (LIBs) have been applied to electronics and electric vehicles (EVs) successfully and their demand is growing. However, limited supply and high cost of lithium (Li) drive the urgent need for alternative battery technologies with more abundant and cost-effective materials. The similar mechanism to lithium-ion batteries (LIBs) and the earth's abundance of sodium (Na) makes sodium-ion batteries (SIBs) a promising alternative[1]. The abundance ratio of Na to Li is 23600 ppm to 20 ppm and processing of battery grade Na is cheaper than Li[1]. Despite high performance, the main bottlenecks of designing safer and long-lasting SIBs are leakage, flammability, and narrow electrochemical window of existing liquid electrolytes with organic solvent. In comparison, solid-state electrolytes offer safety, stability, and high energy density. Therefore, developing high-performance solid-state electrolytes (SSEs) presents one of the most significant tasks in designing safer all-solid-state batteries (ASSBs) with optimum performance.

1.2 Na-ion batteries: an alternative to Li-ion batteries

Abraham (2020) compared the specific energy and energy density of 18650 model commercial Li-ion cells with the Na-ion cells[1]. The LIBs with graphite anode provide a maximum specific energy of 126 Wh/kg against lithium iron phosphate (LFP) cathode while the maximum is 285 Wh/kg against the lithium nickel cobalt aluminum oxide (NCA) cathode. The energy density ranges from 325 Wh/L to 785 Wh/L, NCA cathode providing the highest value in this case as well. Compared to LIBs, the maximum specific energy and energy density recorded for a Pacific Northwest National Laboratory-Washington State University (PNNL-WSU)18650 Na-ion cell is 150 Wh/kg and 375 Wh/L, respectively. Abraham (2015) also compared that the specific energy of conventional Pb-acid, Ni-Cd, Ni-Zn, and Ag-Zn are 30 Wh/kg, 40 Wh/kg, 70 Wh/kg, 75 Wh/kg, respectively which is significantly lower than the Na-ion batteries[2]. If the current Na-ion battery technology is optimized for industrial application, it can substitute

the LIBs with LFP cathode that is being implemented in the light duty electric vehicles, grid scale energy storage systems, and other applications where high energy density is not a requirement. Another advantage of SIBs from the materials criticality viewpoint is the possibility of fabricating the cathode without Cobalt (Co), securing the supply of materials and sustainability[1].

Moreover, the SIBs offer wider operating temperature range as opposed to the LIBs [3]. While the LIBs can operate between -20 and 60 °C, the SIBs are capable of functioning within the -40 – 80 °C range. In addition, the temperature rise during the short circuit is minimal due to higher internal resistance of Na-ion batteries (SIBs). However, the ionic radius of Na^+ (1.02 A) is higher than that of Li^+ (0.76 A) which impedes the diffusion rate of Na^+, and is responsible for the volume effect, the reason why Na-ion batteries have fallen back in the competition with the LIBs in the early 1970s (ref.[3]). Several atomistic simulations, and molecular dynamic studies provided promising insights on Na^+ diffusion mechanisms in materials for application in SIBs (ref.[4]). For instance, a DFT study showed that Na^+ movement in 1T-MoS_2 (a polymorph of MoS_2) could be hindered by the sulfur atoms pointing toward the interlayer spacing when Na−S distances along the path become too small[4].

1.3 Na-ion batteries: working principle and architectures

The SIBs, similar to their counterpart LIBs, operate with the so-called “rocking chair” mechanism. In general, a typical SIB involves the back-and-forth movement of Na^+ between the electrodes to perform the charging and discharging process[5]. During the charging phase, Na^+ are extracted from the cathode and inserted into the anode via the electrolyte. Simultaneously, electrons are transferred to the anode through the external circuit to balance the charge. Conversely, during discharge, Na^+ are removed from the anode and inserted into the cathode through the electrolyte. Na^+ maintain a consistent ionic state throughout their cycling between the anode and the cathode[3,5,6]. Figure 1.1 illustrates the architectures of conventional batteries with liquid electrolytes and the solid-state batteries, using the schematic of a lithium-ion battery as an example.

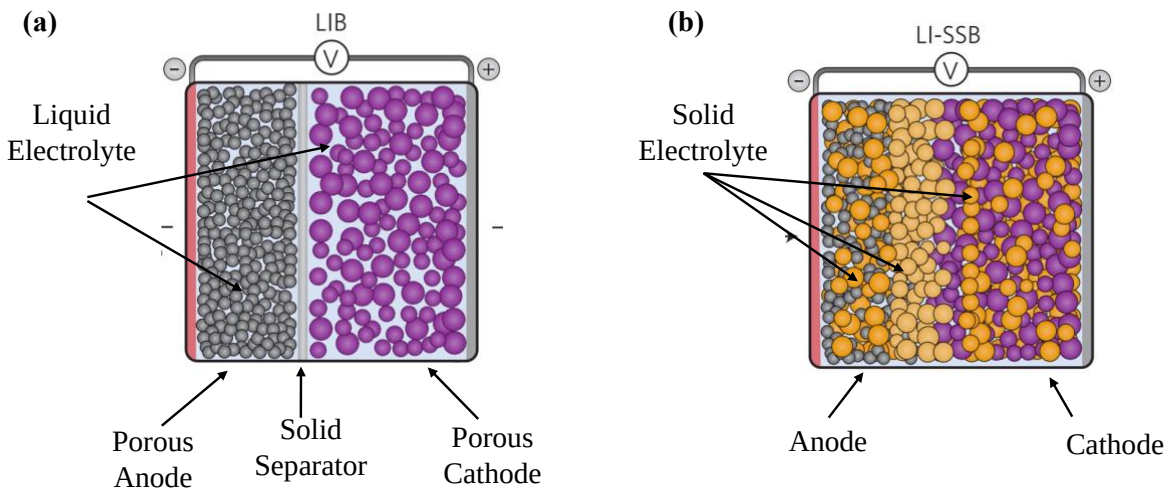

Figure 1.1: Schematic representation of lithium-ion batteries with (a) liquid electrolyte, (b) solid electrolyte[7]. The circles in (a) are grey: porous anode, violate: porous cathode. The grey band in (a) is the thin separator. The light blue part in (a) is the liquid electrolyte wetting the porous electrodes and separator assembly. The circles in (b) are grey: anode, violate: cathode, dark orange: solid electrolyte in the electrodes, orange: solid electrolyte acting as separator.

In conventional batteries a thin separator is placed in-between much thicker and porous electrodes[7]. A liquid electrolyte infiltrates the electrode and separator assembly. Liquid electrolytes wet the entire surface of the electrodes. Current shift to solid-state batteries replaces 1.) the electrolyte-filled separator with the solid electrolyte, 2.) the liquid electrolyte in the electrode with the solid electrolyte[7]. However, the interfacial contact between the electrode and electrolyte in solid-state batteries is more difficult to realize with particle-to-particle contacts. This 2D interfacial contact results in reduced surface contact.

1.4 Choice of solid-state electrolytes (SSEs) for Na-ion batteries

Owing to the potential safety issues from the leakage and flammability of liquid electrolytes, solid-state electrolytes gained significant attention in recent times. The SSEs are classified mainly into three categories: solid polymer electrolytes (SPEs), inorganic solid electrolytes (ISEs), and composite solid electrolytes (CSEs) (ref.[8]). On the one hand, the mostly investigated inorganic electrolytes include sulfides and oxides, here especially β''-Al_2O_3, and sodium superionic conductors (NASICONs). The polymer-based solid electrolytes are mainly polyvinyl fluoride (PVDF), polyethylene oxide (PEO), poly acrylonitrile (PAN) (refs.[8,9]) Each type has its own advantages and limitations. While the ISEs offer enhanced ionic conductivity,

thermal, and mechanical properties, they lack sufficient electrode/electrolyte interfacial contact. In comparison, the polymer-based solid electrolytes offer improved contact at the electrode/electrolyte interface. However, they fall behind the ISEs in terms of ionic conductivity and mechanical strength[9]. This led to the idea of preparing the third type of solid electrolytes: CSEs, which is basically the combination of inorganic and polymeric materials. CSEs offer the mechanical and thermal properties of inorganic ceramic electrolytes and flexibility, and good interfacial contact from polymer electrolytes. The electrochemical properties of some major types of SSEs and their advantages, and limitations are presented in Table 1.1.

Table 1.1: Properties of SSEs used in Na-ion batteries[9].

SSE type	**Materials**	**Conductivity [S cm^{-1}]**	**Electrochemical window [V vs. Na^+/Na]**	**Benefits**	**Limitations**
Boron hydrides	$Na_{2-x}(B_{12}H_{12})_x(B_{10}H_{10})_{1-x}$, $Na_{2-x}(CB_{11}H_{12})_x(B_{12}H_{12})_{1-x}$	10^{-4}–10^{-2}	Up to 5	Thermal and mechanical stability	Limited research, high interfacial resistance
Oxides	Na-β"-Al_2O_3, NASICON	10^{-4}–10^{-3}	Up to 7	High thermal, chemical, and mechanical stability	High grain boundary and interfacial resistance
Sulfides	Na_3PS_4, $Na_{11}Sn_2PS_{12}$	10^{-4}–10^{-2}	Up to 5	Flexibility, mechanical strength, low resistance	Moisture sensibility, low oxidation stability, interfacial resistance
Polymer	PEO-Na salt, PVDF-HFP	10^{-6}–10^{-4}	Up to 4.5	Lightweight, flexible, stable with Na metal	Limited ionic conductivity , thermal and oxidation stability

The above-mentioned Table 1.1 illustrates the lowest ionic conductivity and electrochemical window for the PSEs. In comparison, the newly developed boron hydrides exhibit superior ionic conductivity among all types of SSEs mentioned. However, only few applications in Na-

ASSBs are reported and the research on these types of SSEs are still ongoing. Although sulfide and oxide-based SSEs provide similar ionic conductivity, the sulfides fall behind in terms of electrochemical stability. Moreover, sulfide SSEs are sensitive to moisture, leading to corrosion of the electrodes and increase in interfacial resistance[9]. Among the oxide-based SSEs, the sintering temperature of NASICON (1100 – 1250 °C) is significantly lower than those of Na-β"-Al_2O_3 (~ 1600 °C) (ref.[10]). Considering these electrochemical properties and convenient processability, NASICON was chosen as the SSE for this study.

1.5 NASICON-type electrolytes

The sodium (Na) super ionic conductor (NASICON) type materials ($Na_{1+n}Zr_2Si_nP_{3-n}O_{12}$, $0 \leq n \leq 3$) was first reported by Hong, Kafalas and Goodenough in 1976 (ref.[11]). Since their discovery, this family of materials has been studied extensively owing to their promising chemical/electrochemical and thermal stability in addition to high ionic conductivity. Compounds with NASICON structure offer 3D ion migration framework for Na^+ ions which is formed of the PO_4/SiO_4 tetrahedra sharing the corner oxygen of MO_6 octahedra. They exhibit two dominant crystal structure, namely rhombohedral ($R\underline{3}c$) and monoclinic ($C2/c$) depending on the composition and temperature. The structure is rhombohedral except the composition with $1.8 \leq n \leq 2.2$ and below 160 ˚C when the NASICONs transform to monoclinic phase [9,12]. Apart from these two crystal structures, some NASICONs, for instance $LiZr_2(PO_4)_3$ and $LiSn_2(PO_4)_3$ undergo a triclinic phase transition at low temperature[12]. A schematic of crystal structure of NASICON type materials is presented in Figure 1.2.

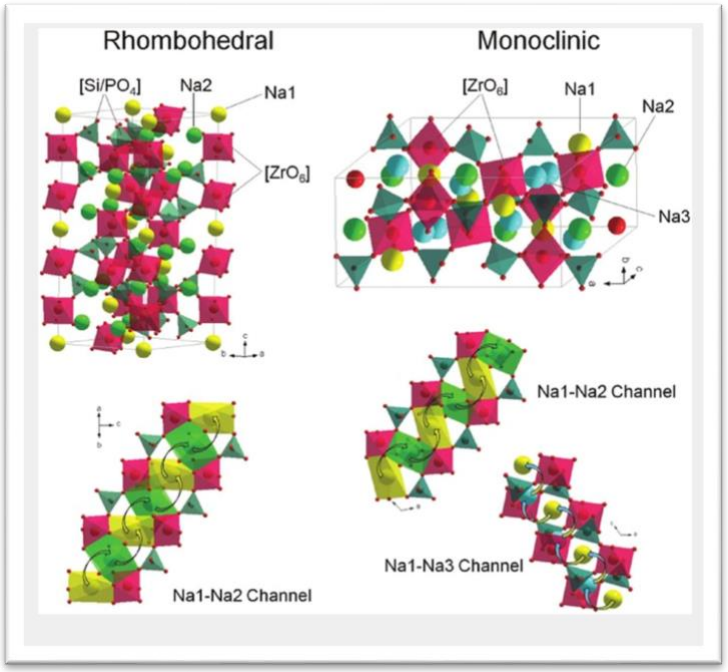

Figure 1.2: Crystal structures of rhombohedral and monoclinic phase NASICON type $Na_3Zr_2Si_2PO_{12}$ and their ion transport paths[13].

The ionic conductivity of the NASICON materials depends on crystal structure, charge carrier concentration, and vacancy sites. Bulk ionic conductivity can be enhanced to 4.0×10^{-3} S cm^{-1} through partial aliovalent cation substitution of Zr^{4+} with Sc^{3+} (refs. [14,15]). Similar effect has been observed by substitution with other metal ions such as Nb^{5+}, Zn^{2+}, La^{3+}, Ni, Mg^{2+}, Y^{3+} [10]. These substitutions increase Na^+ ion concentration, modify the ion migration pathways or create positive charge deficiency without distorting the pristine crystal structure. However, the Na^+ ion concentration needs to be balanced with vacancies in order to reach the maximum result. Ma et al. (2016) reported a maximum ionic conductivity with 3.4 moles of Na in $Na_{1+n}Zr_2Si_nP_{3-n}O_{12}$ (ref.[14]).

1.6 Current state of the art

In recent years, SSEs have become a center of attention for the battery research due to their enhanced safety, durability, thermal stability and potentially high energy density[16]. The SSEs offer the opportunity to avoid safety issues originating from the leakage and flammability of the liquid electrolytes[17]. However, despite their promising advantages, several challenges, for instance poor electrode/electrolyte interfacial contact, lower ionic conductivity, and dendrite

growth are significantly hindering the advancements in developing efficient ASSBs (refs.[16–18]). SSEs with porous structure are potential candidates to address these challenges and several attempts were taken to fabricate SSEs with different porous structure. Kotobuki et al. (2011) designed a 3-dimensionally ordered porous $Li_{0.35}La_{0.55}TiO_3$ electrolyte using a crystal-templating method and supported it with another honeycomb structure made of the same materials[17]. Despite obtaining higher (1.7 times) discharge capacity compared to its nonporous counterpart, the volumetric capacities were identical. The authors identified the irregular arrangement of the porous layers, incomplete loading of the active materials, and geometry (pore diameter and pore wall thickness) as the possible reasons. The irregular pore structure hinders the complete loading of cathode active materials (CAM) which leads to uneven distribution of CAM and reduced electrolyte/electrode surface contact. Moreover, their porous honeycomb structure was characterized by pores with 180 μm in diameter and 80 μm wall thickness, offering long ion migration paths which only increased the internal resistance. Recently, Jaschin et al. (2024) fabricated a 3D porous-dense-porous trilayer and bilayer of NASICON ($Na_3Zr_2SiPO_{12}$) via tape casting method[19]. They used polymethylmethacrylate (PMMA) spheres as the pore former and were able to synthesize electrolytes with pore diameters of approximately 5 to 10 μm (65% void fraction). The thickness of their dense and porous layers was 25 μm and 55 μm (on average) respectively. Their work showed successful infiltration of Na metals used as anode material and enhanced surface contact. However, no cathode infiltration has been performed in this research as it was directed to investigate anode/electrolyte interfacial resistance. The incorporation of Zn^{2+} and Mg^{2+} in NASICON, ZnO nanolayer coating, and tri/bilayer porous architecture brought anode interfacial resistance from 9 Ω cm^2 to 3.5 Ω cm^2 which resulted in an impressively high current density of 40 mA cm^{-2}. In addition, the result showed successful prevention of dendrite growth through maintaining interfacial contact, protective coating, compact dense layer. Zhang et al. (2024) presented the possibility of achieving high cycling stability of 600 h at 0.1 mA cm^{-2} with a garnet-type $Li_7La_3Zr_2O_{12}$ (LLZO) porous electrolyte with pore diameter of 2.3 μm and 65% void fraction[20]. Their SSE structure yielded highest reported specific surface area of 1.3 μm^{-1} till date. Similar approach of tape casting was followed here as well and 1.5 μm monodisperse acrylic particles were used as the pore former. Shen et al. (2020) investigated the feasibility of fabricating porous 3D LLZO electrolyte prepared via freeze tape casting method[21]. Their result showed porous structures up to 75% void fraction with homogeneous distribution of similar sized pores. Subsequent progress of this research demonstrated successful infiltration of

$LiNi_{0.6}Mn_{0.2}Co_{0.2}O_2$ (NMC-622) cathode material into the unidirectional porous scaffold[22]. The SSE and the cathode material were reported to maintain good interfacial contact that resulted in increasing current density (1.2 to 1.8 times) and energy density (1.8 to 2.6 times).

It is evident that well-ordered unidirectionally oriented pores with optimal diameter and pore wall thickness (preferably in the μm range) are desired for enhancing the active material infiltration and ion migration. However, only a limited number of literatures is present on designing porous SSEs for Na-ion batteries.

Conventionally, tape casting is preferred due to its ability to produce large number of electrolyte pellets at a single casting process[19]. From that point of view, developing unidirectional porous layers through freeze tape casting is a convenient and economical way. However, several other methods, for instance anodic oxidation, extrusion, unidirectional solidification, and templating have been reported in the literature[23]. Despite advantages, each of these methods pose their own optimization challenges. The anodic oxidation technique can generate unidirectionally oriented hexagonal array of pores. However, the pores form in nanoscale[23]. Although pore diameter can be controlled within 35 – 470 μm range through extrusion of polymers or pore formers, the structure suffers from discontinuity and disorientation of the pores originating from the thermal decomposition of the pore formers and polymers[23]. Templating is another and considerably mature technology of fabricating ordered 3D and unidirectionally oriented porous microstructures with tunable pore diameter. In the approach presented here, wood is used to mimic its microstructure and to fabricate porous ceramics with similar structure. Unidirectional porous structures with ceramic materials, including AlO_2, TiO_2, SiC, ZrO_2, CeO_2 and several others, have been reported[23]. The unidirectional Al_2O_3 ceramic was fabricated using the bio-templating method by Cao et al. (2004) (ref.[24]). They infiltrated pine and rattan wood as template with low viscous alumina sols and showed the possibility of tailoring the pore diameter between 2 and 200 μm. Uniaxial SiC-ceramic structure was obtained by infiltrating silicon (Si) vapor into pine wood template by Vogli et al. (2002) (ref.[25]). Their technique led to a structure with orderly packed pores of 20 μm and 71% void fraction. Pyrolyzed cork was used as template to prepare mechanically stable 3D CeO_2 ceramic structure with 94.4% void fraction by Novais and Pullar (2019) (ref. [26]). They further showed the tunability of the pore diameter and pore wall thickness by manipulating the number of infiltration cycles and infiltration conditions. Recent advancements in this sector

incorporated the use of three-dimensionally printed sacrificial template. Persembe et al. (2023) used 3D printed PMMA template to obtain yttria-stabilized ZrO_2 (YSZ) ceramic foam with tailored geometry and void fraction higher than 66% (ref.[27]). Okada et al. (2011) reported several composite ceramics, for instance SiO_2/SiC/C, ZrC/C, TiC/C that were fabricated using templating method[23]. However, no such approach was taken to fabricate an electrolyte with unidirectional porous structure for Na-ion batteries. Although tape casting and freeze casting methods were applied to synthesize electrolytes with unidirectionally oriented porous structure, they suffer from incomplete loading of active materials. Therefore, we decided to manufacture unidirectionally oriented structure with the templating method using $Na_{3.4}Zr_2Si_{2.4}P_{0.6}O_{12}$ (NZSP) as solid electrolyte.

1.7 Objective of the thesis

Several questions must be addressed based on the challenges and gaps highlighted in the literature for solid-state ceramic electrolytes for SIBs. This thesis focuses on the development of porous ceramic electrolyte scaffold using the templating method. For this, we addressed the following questions:

1- Can a structure with unidirectionally oriented pores be obtained with NASICON-type electrolyte and a simple and low-cost ceramic processing technique?
2- How much controllable are the pore morphologies? Can the pore diameter and thickness be tuned according to desired goal?

The development of a new electrolyte structure is required to enhance the interfacial contact between the electrode and electrolyte and reduce the ion migration pathway in all-solid-state batteries. Therefore, the goal of this research is to develop an unidirectionally oriented porous electrolyte scaffold for Na-ion batteries. The templating method is followed to obtain unidirectional porous NZSP electrolyte replicating the microstructure of wood. Two different types of wood were selected to investigate the possibility of obtaining different microstructures.

2 Methodology

2.1 Theoretical and experimental background

Several routes of wood template-based ceramics fabrication have been reported[23,28,29]. In general, four process steps, i. e. delignification, pyrolysis, infiltration, and reaction (oxidation or reduction) are followed to obtain porous ceramics using wood template. In one approach, wood is pyrolyzed at 800 – 1500 °C to form highly porous carbon template (CT) which is then infiltrated with preprocessed ceramic sols/slurries/gases/molten compound and subsequently oxidized to remove the carbon template. Another way is to treat the wood chemically with mild acidic or basic solution to remove the lignin (delignification) and other functional groups leaving only the cellulose. The delignified wood is then infiltrated with the ceramic precursors before removing the carbon by oxidation. In this way the ceramic is synthesized inside the template during thermal treatment. Several oxides, including Al_2O_3, TiO_2, Fe_2O_3, Cr_2O_3, ZrO_2 have been prepared using this approach[23]. The former approach is utilized in fabricating non-oxide ceramics and composites like hydroxyapatite, SiO_2/SiC/C, ZrC/C (ref.[23]). While infiltrating the nonreacting sols, it is preferred to pyrolyze the wood before infiltration in order to avoid anisotropic shrinkage due to the thermal treatment[28].

The experimental conditions and parameters, for example chemical reagents, chemical treatment time, pyrolysis media, temperature, dwelling time, heating rate and infiltration method are critical and require precise tuning to obtain the desired porous structure. Jing et al. (2021) used a mixture (4:5 mass ratio) of sodium hydroxide (NaOH) and sodium sulfite (Na_2SO_3) to obtain layered porous hard carbon from balsa wood by dissolving the lignin and hemicellulose for preparing anode materials for sodium ion batteries[30]. The authors showed that this precisely controlled chemical treatment technique adjusted the composition of balsa wood and opened internal functional groups which further enhanced the efficiency of the thermal treatment step. They further studied the impact of chemical treatment duration from 2 to 4 h and pyrolysis temperature up to 1400 °C for natural balsa wood. According to this study, 3 h treatment and dwelling at 1200 °C for 1 h under argon (Ar) flow were found optimal conditions for obtaining the highest void fraction for balsa wood template. In another study, Gao et al. (2021) reported the use of diluted ammonia (5%) solution to delignify poplar wood[31]. The wood samples were treated at 85 °C for 6 h, then they were then washed several times with

deionized water and dehydrated in anhydrous ethanol. A detailed study on the chemical treatment technologies for different wood species, including their composition, chemical reagents, and process conditions are documented in the literature[32]. Novais and Pullar (2019) simply boiled the cork before pyrolysis at 900 °C for 30 min. They used heating rate of 5 °C/min till 150 °C and then increased the rate to 10 °C/min till 900 °C (ref.[26]). They also showed that infiltration is more effective under vacuum (6000 Pa) compared to the isostatic pressure at 20 MPa. Moreover, this work illustrated the possibility of tuning the pore structure by optimizing the number of infiltration cycles. The pyrolysis behavior of cedar wood was studied from 400 to 900 °C with 5 °C heating rate in nitrogen atmosphere by Batailou et al. (2022) (ref.[33]). They reported the development of microporous honeycomb-like structure from 400 – 700 °C with increasing surface area of 310 to 484 $m^2 g^{-1}$. However, the structure is destroyed at 900 °C along with a significant reduction of surface area to 136 $m^2 g^{-1}$.

Therefore, considering the previous studies about experimental conditions, we performed chemical, and thermal studies on selected samples and have chosen the optimal parameters for each step. The overall process is discussed in detail in chapter 3.

2.2 Selection of wood templates

One of the most important considerations is the choice of the right type of wood. Several wood variants, including pine, spruce, poplar, balsa, bamboo, cork (oak bark), and maple have been investigated to obtain the desired pore geometry and void fraction. Compared to the other lignocellulosic woods, cork has the lowest density of 0.12 – 0.24 g/cm^3. Moreover, it possesses ordered microporous structure consisting of hexagonal closed cells with ~20 µm diameter and ~45 µm length[26]. The density of extremely porous balsa wood (0.16 g/cm^3) is close to that of the cork. However, the microstructure varies greatly with the cork in terms of the pore diameter and length. The diameter and length of the tracheid cells in balsa wood ranges from 30 – 70 µm and 550 – 650 µm, respectively[34]. Although the density of american western red cedar wood is comparatively high (0.37 g/cm^3), the pore diameter ranges from 40 to 100 µm and the pore length can be up to 6 mm (ref.[33]). Considering the pore structure, cedar, and balsa wood have been investigated in the present work and finally balsa and cedar have been used as the template for their unidirectionally oriented pores with diameters ranging from 30 to 100 µm.

2.3 Materials characterization methods

The morphological characterization was performed with scanning electron microscopy (SEM). X-ray diffraction (XRD) was performed to check the phase purity. In addition, the pyrolysis and combustion of the wood was studied with the ThermoGravimetric Analysis (TGA) technique. The theoretical background of these analysis methods is presented in sections 2.3.1, 2.3.2, and 2.3.3.

2.3.1 Scanning electron microscopy (SEM)

A scanning electron microscope is a type of microscope that uses a focused high-energy electron beam (usually 0.2 keV to 40 keV) to produce images of a sample's surface. The sample is scanned with a finely focused beam of electrons generated by an electron source and accelerated through a series of electromagnetic lenses. As the electron beam interacts with the atoms in the sample, various signals are generated that can be detected and used to create an image of the surface (Figure 2.1). Auger electrons are very low-energy electrons emitted from the surface of the sample and are characteristic of the elements present. Secondary electrons (SE) are the most common signal used for SEM imaging. SE are generated due to inelastic scattering during the interaction of the electrons with the sample. The SE are low-energy electrons emitted from the sample's surface and detected by a detector located above the sample. Therefore, SE generated from deeper than 10 nm do not possess enough energy after collision to reach the detector. The intensity of the SE signal is proportional to the topography of the sample, allowing the SEM to produce high resolution images of surface features such as pores, cracks, and surface textures. SE electrons only provide information about the surface of the material. In addition to SE, other signals such as backscattered electrons (BSE) and X-rays can also be detected and used for imaging and analysis. BSE signals are generated due to elastic scattering by the interaction of the electron beam with the atoms in the sample and are sensitive to the atomic number and density of the material. X-rays are also generated when the electron beam interacts with the atoms in the sample. The energy-dispersive X-ray (EDX) analysis is yet another useful SEM feature. As illustrated in Figure 2.1, characteristic X-rays can also be detected in a SEM equipped with EDX or wavelength-dispersive X-ray spectroscopy (WDX). EDX is used to map the elemental distribution in the sample and determine their concentration.

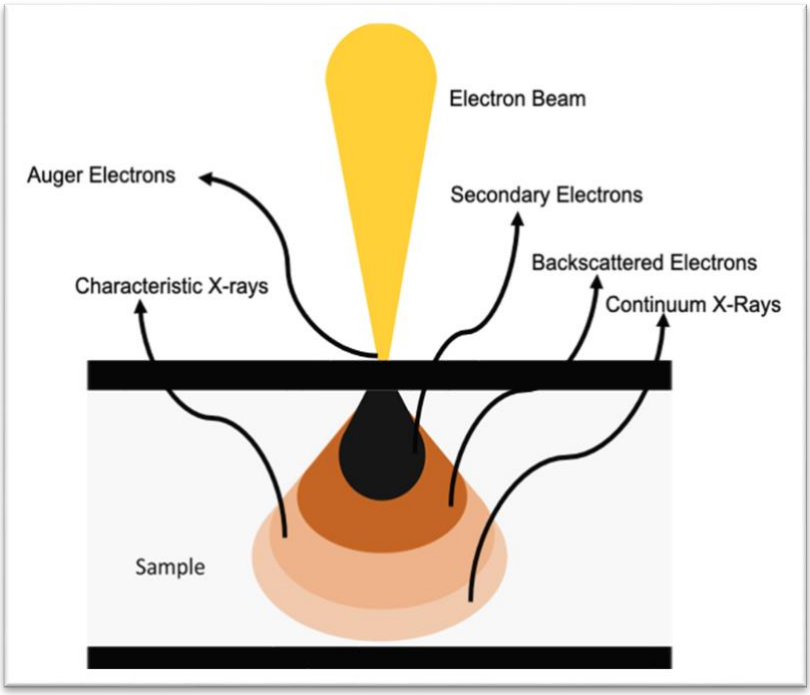

Figure 2.1: Generation of different signals: Auger electrons, secondary electrons, backscattered electrons, and X-rays due to the interaction of the sample with the electron beam.

2.3.2 X-ray diffraction (XRD)

X-ray diffraction (XRD) is a non-destructive technique used to study the structure of materials at the crystal level. When X-rays are passed through a crystalline material, they interact with the atoms in the crystal lattice, causing them to scatter in various directions. The scattered X-rays then interfere with each other, producing a diffraction pattern that can be analyzed to determine the crystal structure. The diffraction pattern is obtained by measuring the intensity and angle of the scattered X-rays. The angle of diffraction is determined by the spacing between the atoms in the crystal lattice and the wavelength of the incident X-rays. This relationship is described by Bragg's law given in the following Equation 2.1 which states that the path difference between the scattered X-rays must be an integer multiple of the wavelength of the incident X-rays to generate constructive interference.

$$n\lambda = 2d\sin\theta \qquad \text{Equation 2.1}$$

where θ is the angle between the atomic plane and X-ray or the Bragg angle, d is the interplanar distance, λ is the wavelength of the incident X-ray and n is a positive integer number. It is important to know that scattered X-rays generating only constructive interference that satisfies

Bragg's condition show intensity in a diffraction pattern. Information about the structure of the materials can be found by determining the collection of interplanar distances. In a diffractogram, material with higher crystallinity shows a sharper peak whereas material with lower crystallinity shows a broader peak. For amorphous materials, no significant peaks can be observed in XRD.

2.3.3 ThermoGravimetric Analysis (TGA)

ThermoGravimetric analysis (TGA) provides useful information on the physical and chemical properties, including absorption, adsorption, desorption, chemisorption, chemical reaction and thermal decomposition of materials under thermal treatment. TGA is used to study the thermal stability, upper working temperature limit, and kinetics of thermal degradation of materials among many other uses. The mass change is measured against temperature over a defined duration of time when the samples undergo continuous temperature change. The thermogravimetric analyzers measure this mass change with the help of precision thermobalance placed under the sample pan. The TGA curve is obtained by plotting the mass or the percent change of the mass in the y-axis and temperature in the x-axis. Different atmospheres, for instance air, corrosive, carburizing, and inert gases are coupled with tunable vacuum, high or constant pressure system depending on the final goal. While inert gases, for example nitrogen (N_2), hydrogen (H_2), argon (Ar) are used in pyrolytic studies, air is suitable for studying the combustion kinetics.

In this research, TGA of both raw and pyrolyzed wood has been performed to study their pyrolytic and combustion steps, respectively. The pyrolysis of raw wood was studied in inert media maintained through purging pure Ar, whereas pyrolyzed carbon was studied in air to check the final temperature until the full combustion takes place. The measurements were performed with the simultaneous thermal analyzer NETZSCH STA 449 F3 Jupiter® between room temperature and 1600 °C with a heating rate of 5 °C/min.

3 Experimental procedure

3.1 Materials, chemicals and reagents

Western red cedar (20 mm in diameter), balsa (20 mm), and cork (25 mm) were purchased from eBay online shopping platform. The chemicals including ammonia (NH_3), sodium hydroxide (NaOH), sodium sulfite (Na_2SO_3), ethanol (EtOH), methylethyl ketone (C_4H_8O), polyvinylbutyral (PVB-98, $(C_8H_{14}O_2)_n$) were purchased from Sigma-Aldrich. All the chemicals were analytical grade and used without additional purification. NZSP powder with the nominal composition $Na_{3.4}Zr_2Si_{2.4}P_{0.6}O_{12}$ was received from Dr. Qianli Ma (IEK-1) and used to infiltrate the pyrolyzed balsa and cedar wood after preheating it at 900 °C for 4 h. After this heat treatment the powder is still predominantly amorphous.

3.2 Steps of experiment

3.2.1 Carbon template preparation

The carbon template preparation includes cutting, chemical treatment (delignification), drying, and pyrolysis (carbonization) of the wood. At first, the selected woods were cut with wire saw perpendicular to the axial direction with 1 to 2 mm thickness to open the unidirectionally oriented porous structure of the wood. In order to obtain a smooth cut without damaging the opening of the pores, the speed of the wire saw, and pressure load were carefully optimized. In general, the wire saw was operated at 1.7 m/s with a weight load of 250 g. These wood pieces were then treated chemically for 3 h at 85 ºC in a mixture of sodium hydroxide and sodium sulfite (4:5 mass ratio). A separate treatment method using 5 vol% ammonia solution was also used in the delignification step. These delignified samples were soaked into an anhydrous ethanol solution for gradual dehydration; the treatment was then followed by oven drying at 80 °C for 12 h. The dried balsa wood pieces were pyrolyzed in argon at 1200 °C for 1 h. A separate pyrolysis condition was followed for the cedar wood as the cell walls start to break above 800 °C as reported by Batailou et al. (2022) (ref.[33]). The heating rate for both cases was same, 5 °C/min up to 150 °C and then 10 °C/min up to 800 °C (cedar) and 1200 °C (balsa). At this point, the woods were fully pyrolyzed leaving only the carbon template and were named as pyrolyzed wood.

3.2.2 Infiltration

At first, a slurry was prepared with 25 wt% solid content including NZSP, binder (PVB98) and dispersant as mentioned in Table 3.1. The slurry preparation starts with mixing the dispersant with the solvent composed of 33 wt% EtOH and 67 wt% methylethylketone (MEK). The ingredients were then mixed in a planetary mixer for 2 min at 1500 rpm and 101.1 kPa. Following this mixing process, 1 g of zirconia balls (40 wt% 3 mm and 60 wt% 5 mm in diameter) and 0.1 g of binder, polyvinyl B (PVB98), were added sequentially. Then the above-mentioned mixing step was repeated three times in the planetary mixer. The mixture was then placed on a roller bench overnight for obtaining a homogeneous slurry. This slurry was degassed in vacuum (20 kPa) for 30 min before it was finally ready to be infiltrated in the carbon template.

Two different types of infiltration procedures (atmospheric and vacuum) were performed. In atmospheric infiltration method, the slurry was dropped on the carbon templates with syringe. However, in vacuum infiltration method, the carbon templates were completely soaked in the slurry contained in a beaker. The beaker was then placed in a 250 mm (internal diameter) desiccator and infiltration was performed at 20 kPa (80% vacuum system) for 10 min. The infiltrated/impregnated carbon templates were then dried for 12 h at 85 °C before sintering.

Table 3.1: Composition of the NZSP slurry.

Materials	**weight (g)**	**wt% (overall)[1]**	**wt% (With respect to ceramic)[2]**
NZSP	1.0	24	-
Solvent	3.0	72	300
Dispersant	0.04	0.97	4
Binder	0.1	2.42	10
Zirconia balls	1	-	100

[1] The overall wt% denotes the weight fraction of the components with respect to the overall weight of the slurry.
[2] The wt% with respect to ceramic denotes the weight fraction of the components with respect to the weight of the NZSP powder in the slurry.

3.2.3 Sintering

The dried infiltrated carbon templates were sintered in air at 1265 °C to obtain the desired NASICON phase. The infiltrated templates were placed on a platinum foil to avoid any side reaction originating from the substrates. As the carbon templates contained carbon and organics (PVB) along with NZSP, a two-step heating was performed. At first, the heating rate was set to 2 °C/min till 800 °C and set to dwell for 2 h to facilitate the combustion of the organics and carbon. From this point, temperature was increased at a rate of 5 °C/min up to 1265 °C to form the final NASICON phase.

Therefore, the overall process is as follows: cutting of wood along radial direction, delignification, carbon template preparation through pyrolysis of wood, ceramic infiltration with a slurry, and sintering in air. The process scheme is illustrated in Figure 3.1 below.

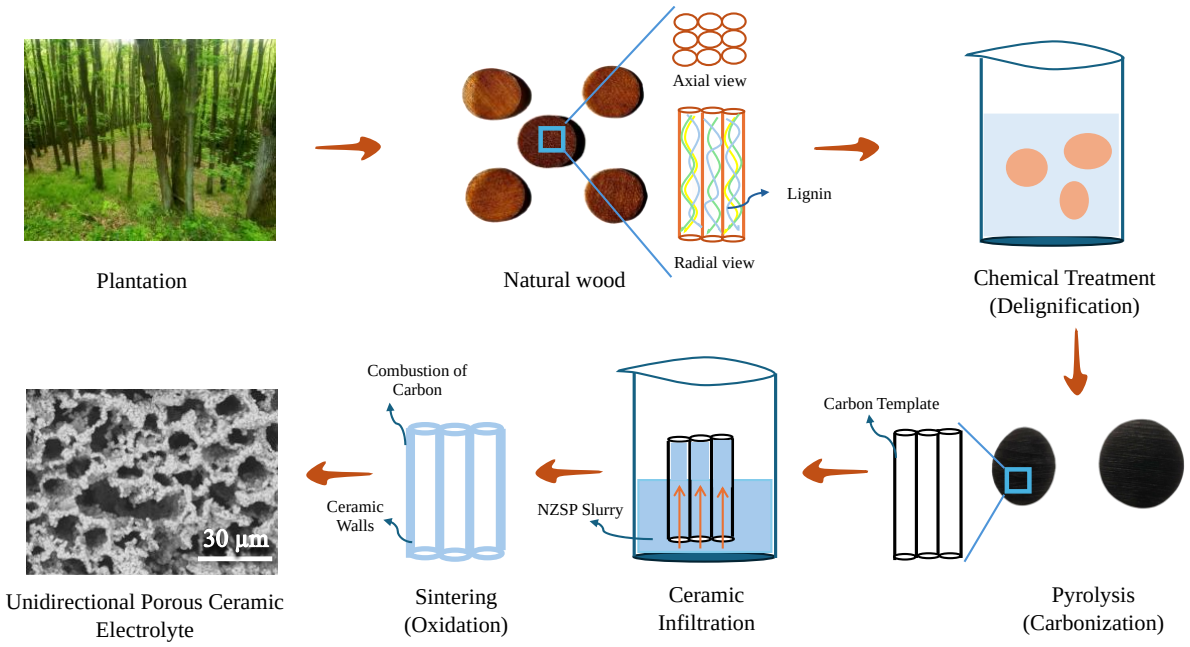

Figure 3.1: Experimental process steps for fabricating porous ceramic electrolytes using wood template.

3.3 Sintering support preparation

The sintering supports made of made of NZSP were prepared for performing the sintering of infiltrated carbon templates. Two different types of sintering supports were prepared. The first one was prepared with only NZSP powder while the second variant of NZSP powder contained 0.5 wt% PVB as binder. For the latter case, 5 wt% of PVB was added in 10 ml EtOH which was then mixed with 100 g of calcined NZSP powder. 4 g of these powders were pressed at 20 kN for 2 min in a unidirectional hydraulic press. The resulting pellets (50 mm in diameter with a thickness of 3 mm) underwent the sintering process at 1280 °C for 4 h in air.

3.4 Materials characterization

The phase purity of the prepared porous NZSP electrolyte was investigated by XRD with a Bruker D4 ENDEAVOR X-ray diffractometer with Cu $K_{\alpha 1}$ source (wavelength 1.54 Å). XRD patterns of the samples were recorded with a scan rate of 1 scan per 47 min over a range of 10 to 80 degrees (2 theta range) with step size of 0.02 degrees. The morphology of the materials was observed with a Hitachi TM3000 field emission scanning electron microscope. SEM images were captured using a 5.0 keV acceleration voltage, 10 µA emission current at a working distance of 8.7 mm to 8.8 mm for the electrolyte material. As the NZSP ceramic was non-conductive, a thin layer gold was sputtered on the sample before SEM analysis. The particle size distribution (PSD) was measured in ethanol using Horiba LA-950V2 laser diffraction analyzer. The void fraction of the sintered electrolytes was measured in ethanol system following the Archimedes method.

4 Results and discussion

The result and discussion section is split in three subsections: section 4.1, section 4.2, section 4.3. The section 4.1 presents the studies on carbon template preparation, while NZSP powder processing and infiltration is included in the subsection 4.2. And the last section (4.3) presents the sintering studies of the porous NZSP ceramic.

4.1 Carbon template preparation

As mentioned earlier in this report, carbon template preparation includes cutting, chemical treatment, and pyrolysis of wood. In this section, detailed results and observations are included.

4.1.1 Unravelling the microstructure of wood

The process of cutting the wood, despite being simple, is one of the most challenging and important steps of wood template based ceramic preparation. In this research, it was decided to reach the thickness of 1 mm, and the wood was required to be cut perpendicular to the axial direction of the wood in order to obtain the porous structure. Several methods, including wire saw, laser cutting, water jet or sharp knife are various possibilities to cut the wood pieces with precision thickness. Soft woods, for instance balsa, can be easily cut with ordinary knife or razor blade. However, equipment, for instance sharp knife, exerts pressure on the wood, significantly damaging the shape of the pore openings. Due to the thickness of the knifes, it is also not a convenient method to perform cutting without breaking the wood into smaller pieces. Moreover, the precision in thickness is lost along with damaging the wood structure. To avoid such inconveniences, it was decided to cut the wood pieces with wire saw where precision up to ± 5% can be reached. The average thickness of 1 mm was obtained reproducibly without applying noticeable amount of force on the wood. However, this technique proved not to be sufficient alone as the wire saw is not sharp enough to cut through the wood smoothly. The 65 µm wire saw twists the surface of the wood leaving a rough fiber-like structure that closes the pore openings completely. The following Figure 4.1 shows the cutting process.

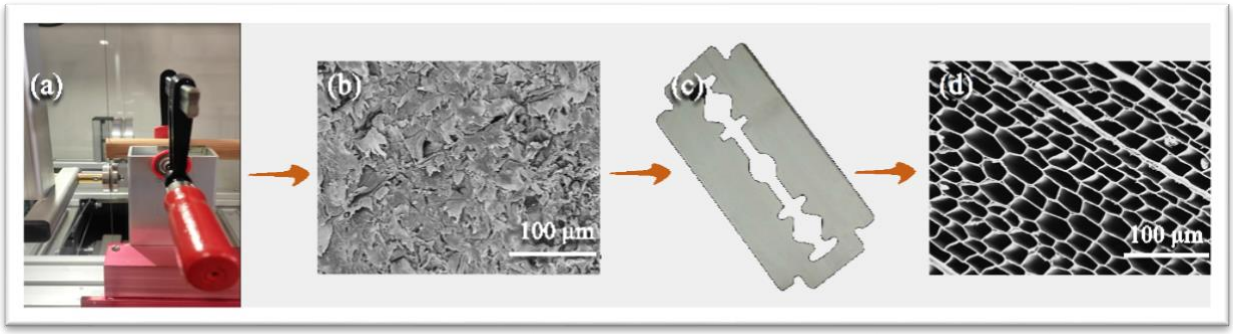

Figure 4.1: The complete wood cutting process. (a) Cutting of wood using wiresaw along the radial direction, (b) the sliced wood's surface structure, (c) shaving the surface of sliced wood with sharp razor blade, (d) microstructure of the surface after shaving with razor blade.

Figure 4.1 (b) shows the SEM image taken from the surface of the cedar wood piece after cutting with the wire saw shown in Figure 4.1 (a). The image in Figure 4.1 (b) clearly shows no sign of pores which sharply contrasts with the theoretical knowledge about wood anatomy. This challenge is solved by simply shaving the surface with sharp razor blade showed in Figure 4.1 (c). For this treatment, the woods are boiled in distilled water for 10 min. The dry cell walls of the wood swell up, absorbing the moisture, and become soft. Then, shaving the rough surface with sharp razor blade unraveled the pores without damaging the openings.

The cutting step is one of the most important steps as to ensure open channels for the ceramics to penetrate the wood template. The closed pores stay closed even after pyrolysis, ultimately making it impossible for the ceramic particles to infiltrate. Therefore, special attention should be given while cutting the wood. Other high-tech cutting technologies, for example laser or water jet were not investigated in this study. However, one can suspect that laser cutting will oxidize the wood samples in air and water jets will exert force on it.

4.1.2 Chemical treatment

In this section, the influence of chemical treatment on the wood samples for delignification is focused. More detailed discussion on the wood anatomy and chemical treatment technologies for different types of woods based on different goals can be found in literature[32]. The wood cell walls of vessels and tracheid forming the pores are mainly composed of cellulose, hemicellulose, and lignin. The cellulose materials provide the frame of the porous structure

while the hemicellulose and lignin form layer around it and play an important role in enhancing the mechanical stability. In this study, the primary goal of this delignification step is to selectively remove the lignin and hemicellulose to reduce the cell wall thickness and increase the pore diameter. As mentioned earlier, two different chemicals, for instance, a mixture of 4:5 mass ratio of NaOH and $NaSO_3$, and 5% ammonia solutions were tried separately to check their effect on the mechanical stability of the wood. However, this type of chemical treatments reduces the mechanical strength and causes excessive shrinkage of the pyrolyzed carbon template. This reduced strength makes the carbon templates breaking and falling apart. The reason is well explained by the TGA performed on the (delignified and raw) balsa wood. The TGA results are presented in section 4.1.3. Therefore, the chemical treatment step is excluded from the experimental procedure and the woods were pyrolyzed directly after shaving with the razor blade.

4.1.3 ThermoGravimetric Analysis (TGA)

The TGA of raw wood was performed in argon (Ar) while the pyrolyzed carbon template were analyzed in air. TGA provided information on thermal decomposition of both woods during pyrolysis, and sintering. In addition, this analysis provided useful information on the effect of chemical treatment on the wood. The results are presented in Figure 4.2.

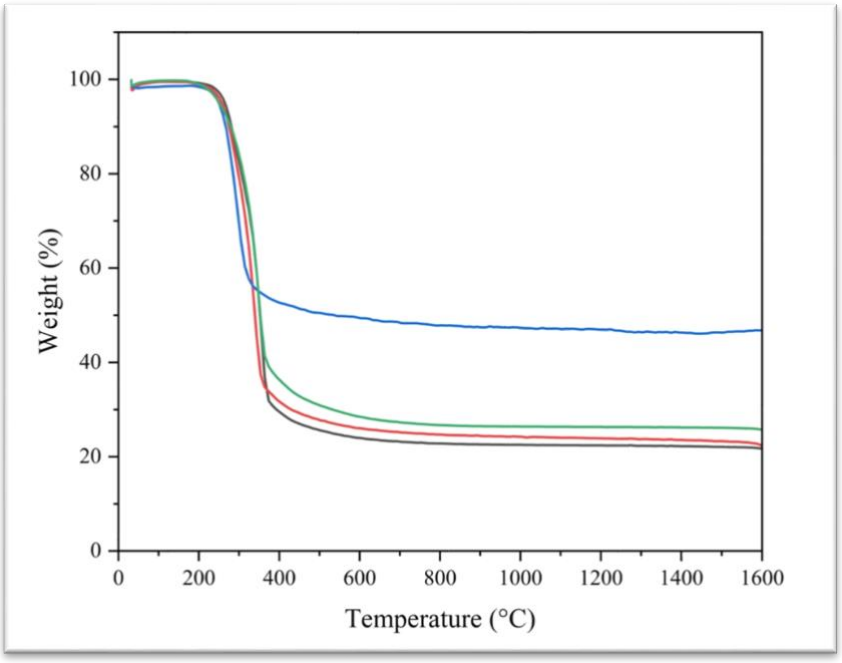

(a)

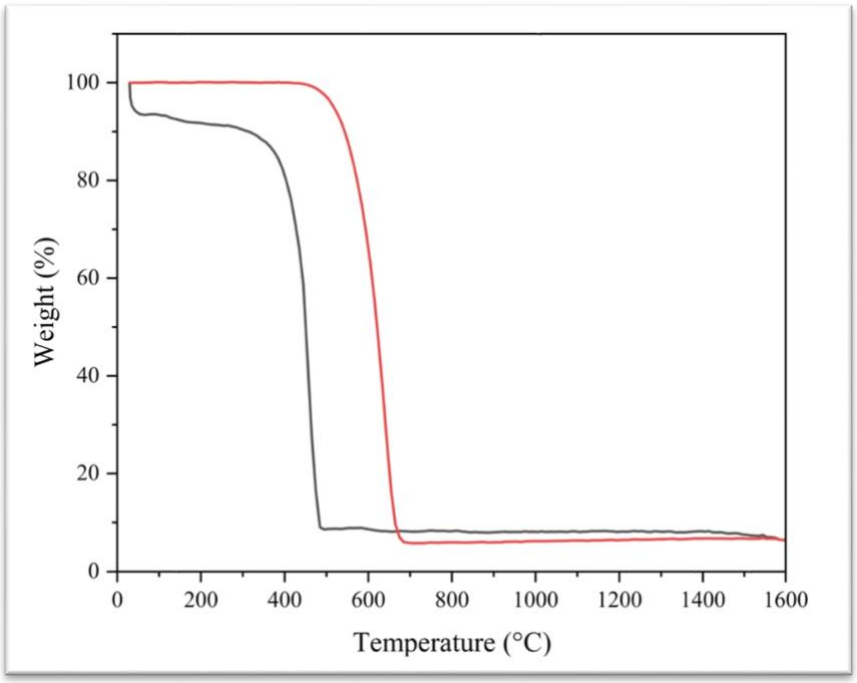

(b)

Figure 4.2: ThermoGravimetric Analysis of (a) balsa (both chemically treated and untreated) and cedar in argon (Ar), (b) balsa and cedar in air. The lines in (a) black: ammonia treated blasa, red: sodium hydroxide and sodium sulfite treated balsa, blue: raw balsa (untreated), and green: raw cedar (untreated). The lines in (b) black: pyrolyzed balsa, and red: pyrolyzed cedar. x-axis: weight (%), y-axis: temperature (°C).

The TGA in argon (Ar) presented in Figure 4.2(a) reflects the thermal process performed during the pyrolysis of raw wood to form the carbon template. The raw balsa (blue line) wood lost around 45% of its weight. The chemically treated woods lost more than 75% of their weight. This excessive mass loss is the reason of mechanical strength loss for the chemically treated balsa. Despite varying weight loss, all of the woods (including cedar in green line) were fully decomposed below 700 °C. The weight loss of cedar was around 70%. Unlike the balsa templates, cedar template did not lose its mechanical strength beyond working limit.

The TGA in Figure 4.2(b) illustrates the thermal decomposition kinetics of the pyrolyzed carbon templates in air. This study reflects the scenario that takes place while sintering the infiltrated carbon templates. The grey line represents the weight loss of balsa while the red line represents the weight loss of cedar upon pyrolysis. The balsa template burned completely at around 500 °C while complete combustion of the cedar template took place at around 700 °C. Despite this minor difference, both infiltrated templates were sintered together up to 1250 °C with an intermediate step of 2 h at 800 °C to ensure complete combustion of the carbon templates and other organics used in the slurry.

4.1.4 Microstructure analysis of pyrolyzed wood

After cutting the raw wood pieces with wire saw, the porous structure of the two types of woods, i.e. balsa and cedar was uncovered beneath the fibrous surface with razor blade. After pyrolysis, the pore structure of the selected woods was investigated by SEM and the SE images with different magnification are presented in Figure 4.3.

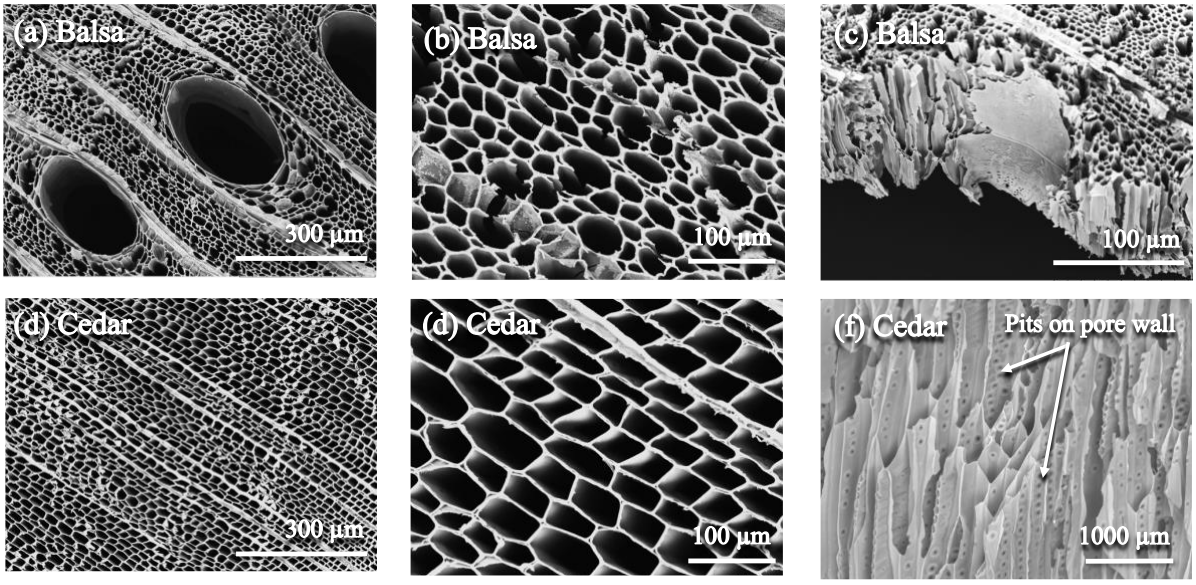

Figure 4.3: Microstructure of (a – c) pyrolyzed balsa wood, (d – f) pyrolyzed cedar wood.

The balsa wood is characterized by three different types of pores, namely large, medium, and small. The large elliptical pores have diameters in the range of d_{short} = 150 – 190 µm and d_{long} = 250 – 300 µm and are distributed homogeneously across the sample. The space in-between the large pores is filled with the medium and small pores. The medium pores have diameters of 20 to 50 µm while those of the smallest ones are 2 to 10 µm. The smallest pores are basically formed in between the medium pores. The medium pores play the key role in ceramic structure formation because of their predominant presence. The fracture surface perpendicular to the axial direction (Figure 4.3(c)) was examined to detect any potential micro or nanopores and study the interconnectivity of the adjacent cells. However, no such interconnecting structure elements was observed. The pore wall thickness was observed to be around 1 to 2 µm.

In comparison to balsa, cedar has considerably different packing of pores and the earlywood region of the cedar exhibits pores of 30 to 60 µm in diameter with some of the pore diameter exceeding 80 µm. The cedar microstructure is dominated by the medium-sized pores. Whereas the pores in the balsa wood are predominantly elliptic, the cedar wood is built up of rectangular pores like a bricklayer. Apart from this, one of the most interesting features of the cedar is its interconnecting cell walls. The fracture surface shown in Figure 4.3 (f) illustrates the presence of continuously distributed pores (pits) on the cell walls from top to the bottom. The pits on the cell walls have diameters of approximately 2 to 3 µm. In addition, the pore wall thickness

is about 3 to 4 μm. Therefore, the cedar offers the most promising structure to fabricate the porous interconnected ceramic structure.

4.1.5 Thermal behavior of wood during pyrolysis

This section includes a detailed discussion of the behavior of the wood samples during drying and pyrolysis. The physical changes, for instance size, and shape of the wood samples during drying and pyrolysis are important factors in deciding the final shape of the electrolyte scaffold.

Drying is an important step before pyrolysis to remove the moisture content as much as possible. During this process, the wood samples undergo both anisotropic shrinkage and bending which affects the shape of the final ceramics as well. These effects are simply explained with the varying moisture distribution throughout the sample[35]. The moisture evaporation on the surface of the wood pieces is faster than in the inner parts of the wooden piece. This anisotropic moisture gradient induces shear force causing the bending of the sliced wood specimens. Moreover, with decrease in moisture content, the wood reaches a moisture level below the fiber saturation point leading to shrinkage[35]. In the case of present study, although shrinkage was negligible during drying, significant bending took place and let to the deformation of wood. Around 1% and 2% shrinkage in the radial and axial direction was observed for the balsa, respectively. Similar to balsa, cedar also experienced a contraction of around 1% both radially and axially.

Similar type of tangential bending was observed for both balsa and cedar. However, balsa displayed a higher degree of deformation. The bending was caused by the horizontal shear force originating from the varying moisture gradient between the surface layers and the bulk of the wood pieces. A schematic illustration of bending mechanism is presented in Figure 4.4 (a).

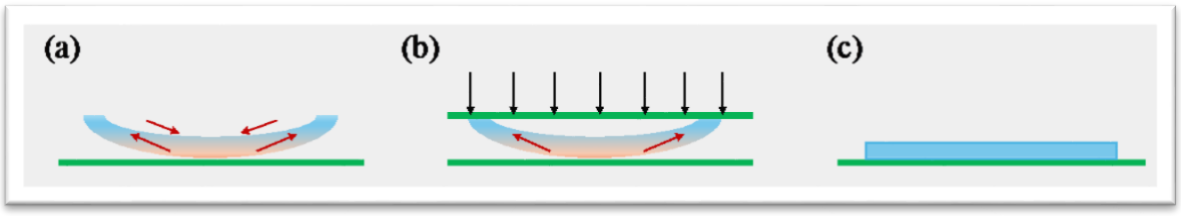

Figure 4.4: Schematic representation of (a) bending during both drying and pyrolysis, (b) weight mounted on the wooden disk, (c) flat wooden disk after pyrolysis.

Both balsa and cedar experienced this bending and ultimately shape deformation even after treating them with a combination of solvent and vacuum drying. As a further step, the wood pieces were sandwiched between two flat surfaces as illustrated in Figure 4.4 (b). The weight of the substrate mounted on top of the wood piece exerted a force parallel to the axial direction and counteracted the shear force causing the samples to bend. As illustrated in Figure 4.4 (c), flat wood pieces were obtained in this way. The weight of the top substrate should be carefully selected as it might distort the openings of the pores if the substrate is too heavy or inadequate if too light. The energy balance between the shear force and substrate weight is neither studied here nor it was a goal of this work. Therefore, the weight was chosen from the experimental trials and optimized according to the sample type. A rectangular 25 mm × 25 mm × 3 mm alumina crucible was used for the balsa disks. This weight was inadequate given it did not counteract the shear force generated by the cedar. The higher shear force of cedar is probably due to its higher mechanical strength. Another approach was used and found useful in protecting the cedar pieces from bending. Instead of using weight, the cedar pieces were sandwiched in-between to flat pieces of sieve nets and tied with rubber bands. This method yielded desired flatness with negligible bending. The latter approach is applicable to both type of woods. Another possible, however, undesired approach to prevent the bending would consist in increasing the thickness of the samples. As our goal is to reach a thickness below 1 mm, this idea, was not found to be adapted in our context, thereby discarded.

Sufficient removal of the moisture content during the drying step will prevent the samples from bending during pyrolysis and developing fractures leading to damage of the entire cell walls along the axis. Other drying techniques, for instance supercritical CO_2 drying, freeze drying,

superheated steam drying, and cyclic drying should be investigated as they might be useful in controlling the shape and maintaining the microstructure of the wooden pieces.

After drying, the wood samples underwent carbonization during the pyrolysis step. The residual moisture evaporates, and organics decompose leaving the carbon template due to the heat treatment in inert or reducing atmosphere. Changes including overall shrinkage, and crack formation in the carbon template have been studied after the pyrolysis step. Most importantly, severe damage on the balsa was observed as a consequence of the combined drying and pyrolysis process. The initial shear force causing the bending during drying increased during the pyrolysis resulting in an even stronger bending taking the form of an "U" shape. This stronger shear force led to formation of cracks. The crack formed only on the convex surface and no such damage has been observed on the concave surface of the samples. More specifically, only the balsa wood underwent such crack formation. Although the cedar was found to bend, no crack appeared in any of the concave or convex part of the surface. The Figure 4.5 illustrates the surface morphology of balsa with cracks on the surface.

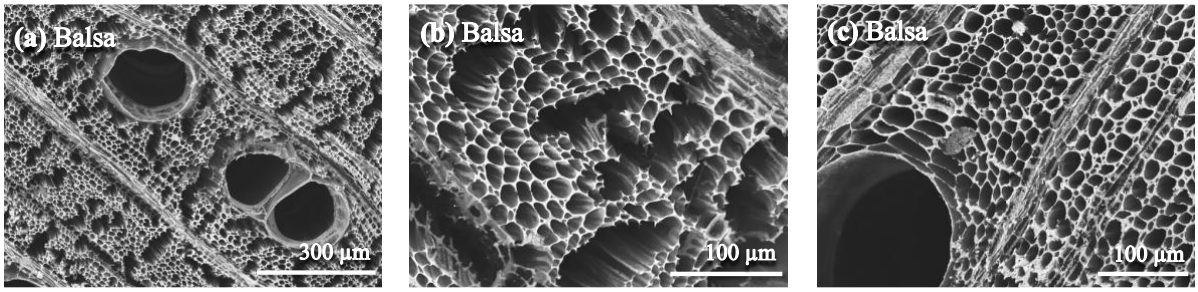

Figure 4.5: Observation of fractures at the surface of pyrolyzed balsa. (a) and (b) Convex surface of balsa, (c) concave surface of balsa.

The Figures 4.5 (a) and (b) present the convex surface of the balsa which is severely damaged due to the formation of numerous cracks. Those cracks disrupt the continuity of the porous structure along both the radial and axial directions resulting in large pores. In comparison, no such cracks have been observed on the opposite surface as illustrated by Figure 4.5 (c).

The overall shrinkage of both balsa and cedar woods was investigated after pyrolysis. The balsa underwent around 27% and 40% contraction in axial and radial direction, respectively, whereas the diameter and thickness of cedar decreased by 35% and 31%. An overall volume reduction of 68% and 71% was observed for balsa and cedar, respectively.

4.2 NZSP powder processing and infiltration into carbon template

4.2.1 NZSP powder processing

Understanding the powder properties and its processing is an essential step in this work. Therefore, special attention has been given to understand the NZSP powder and its properties; then processing is discussed in this section. The NZSP powder with composition ($Na_{3.4}Zr_2Si_{2.4}P_{0.6}O_{12}$) was used to infiltrate the wood templates.

As received, the calcined NZSP had a primary surface area of 17.8 m^2/g. However, for slurry preparation a surface area below 10 m^2/g is suitable. Therefore, a post-processing by heat treatment (post-processed) was performed to study the impact on surface area. The NZSP powder was introduced in an alumina crucible with lid and heated in air at 900 °C for 4 h with a constant heating rate of 5 °C/min and a surface area of 1.3 m^2/g was obtained (see also Table 4.1).

In addition, the post-processed NZSP was ball milled to study any further potential influence of ball milling on the particle size and surface area. The post-processed NZSP was ball milled for 24 h in 48 cycles of 30 min each (5 min of milling and 25 min of intermittent cooling) in a 45 mL stainless steel jar with a mixture of 3 mm (60%) and 5 mm (40%) zirconia balls in ethanol. The milling was performed in a Fritch Advanced Ball Miller. A rotation speed of 500 rpm was used for all the cycles for the milling. The weight ratio of NZSP powder and solvent was kept at 1:3 (15 g of ethanol for 5 g of powder). In total, 70 g of zirconia balls were used. After ball milling, the NZSP (post-processed and milled) was dried, and the powder was recovered for examination of the surface area and particle size distribution. The median particle size distributions (μm) and BET surface areas of three differently conditioned (calcined, post-processed, and post-processed and milled) NZSP powder is presented in Table 4.1.

Table 4.1: Median particle size distribution and BET surface area of NZSP powder.

NZSP	Median Particle Size Distribution (μm)	BET Surface Area (m^2/g)
Calcined	0.61	17.8
Post-processed	7.1	1.3
Post-processed and milled	10.3	14.9

As presented in Table 4.1, the surface area of the preheated and milled NZSP powder increased after ball milling from 1.3 m^2/g to 14.9 m^2/g.

The particle size distribution of the calcined, post-processed and post-processed and milled powders were also measured to check any potential agglomeration that might be larger than the pore diameter of the balsa and cedar wood. Agglomerated particles larger than the obtained pore diameter will block the pore openings and ultimately hinder the infiltration. The PSD results of the calcined, preheated, and preheated and ball-milled NZSP powder is presented in Figure 4.6.

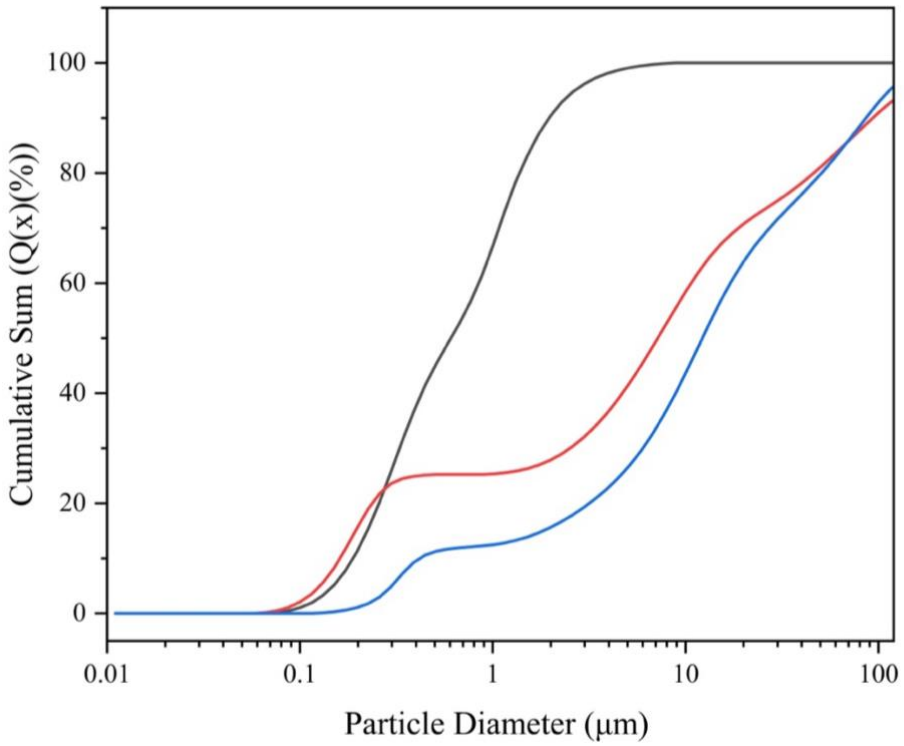

Figure 4.6: NZSP particle size distribution. The lines are black: calcined, red: preheated and blue: preheated and milled. x-axis: particle diameter (μm), y-axis: cumulative sum (Q(x)(x%)).

The calcined NZSP powder (black line) shows a median particle size (d_{50}) of 0.61 µm and a d_{90} of 2 µm. This means that 50% of the particles are smaller than 0.6 µm and 90% of the particles are smaller than 2 µm which would be a very suitable PSD for infiltration. However, after the preheating step the d_{50} value increased to 7.1 µm (red line). Despite this increment, approximately 30% of the NZSP particles stayed below 3 µm. Further, ball milling increased the particle size and a d_{50} of 10.3 µm was obtained. The increment in particle size after ball milling can be attributed to agglomeration of the powder during drying process after the ball milling step. Due the increase in both surface area and particle size, ball milling step was not performed any further. Instead, the post-processed powders were used to prepare the slurry.

4.2.2 Infiltration of NZSP into carbon template

Infiltration of the NZSP slurry into the carbon template plays a crucial role in realizing the scaffold structure and requires thorough understanding of the process. A comparative analysis on the key factors, such as the slurry composition, infiltration method, and number of infiltration cycles is discussed in this section.

For the preparation of the ceramic slurry, the content of solid, dispersant, and binder determine its rheological properties and decides about the success of ceramic infiltration into the pores. The study of the slurry rheology is beyond the scope of this research and was not studied. Instead, the optimization of the slurry composition was based on experience and pre-existing know-how. On the one hand, increasing amount of NZSP powder will tend to agglomerate and form larger particles, ultimately blocking the pore openings. On the other hand, lower amounts will lead to nonhomogeneous deposition of the ceramic on the walls of the carbon template, requiring increased number of infiltration cycles. The amount of dispersant is another important factor as it plays the role of preventing agglomeration by maintaining the distance between the particles[10]. However, excess of the dispersant causes foaming which forms bubbles in-between the liquid and the carbon template. The bubbles act as a barrier and severely hinders the mass transport of the ceramic slurry into the carbon template. The foaming can be reduced by controlling the amount of dispersant in the slurry. An amount of around 4 wt% of dispersants (with respect to the powder content) was optimized. The binder (PVB) is also an important component of the slurry as it prevents sedimentation of the ceramic particles in the slurry

through closely holding them and controls the viscosity of the slurry[10]. Higher binder content increases the viscosity of the slurry while lower amounts cause the particles to settle down which affects the stability of the suspension. The binder content also impacts the ceramic structure, as mentioned in section 4.3 along with the sintering studies. The composition of the initial slurry is mentioned in Table 3.1 and the optimized slurry is presented below:

Table 4.2: Composition of optimized slurry (5 wt% binder)

Materials	**weight (g)**	**wt% (overall)[3]**	**wt% (with respect to ceramic)[4]**
NZSP	1.0	24.4	-
Solvent	3.0	73.35	300
Dispersant	0.04	0.98	4
Binder	0.05	1.2	5
Zirconia balls	1	-	100

To keep the slurry preparation as simple as possible, only the binder was adjusted based on the results after infiltration and sintering. It is to be note that from now on, the initial and optimized slurry composition will be referred to by using the binder content.

At first, the slurry composition documented in Table 3.1 (10 wt% binder) was used to infiltrate both carbon templates. Both types of infiltration (atmospheric and vacuum) were performed with this slurry. The atmospheric infiltration was performed at atmospheric pressure. In this method, the slurry was dropped on the carbon template with syringe. Vacuum infiltration was performed under vacuum (20 kPa). The carbon templates were soaked in the slurry and were kept in the desiccator under vacuum for 10 min. The microstructural images of atmospheric infiltrated carbon templates (both balsa and cedar) and vacuum infiltrated carbon templates (both balsa and cedar) are presented in Figure 4.7 and 4.8, respectively.

[3] *The overall wt% denotes the weight fraction of the components with respect to the overall weight of the slurry.*
[4] *The wt% with respect to ceramic denotes the weight fraction of the components with respect to the weight of the NZSP powder in the slurry.*

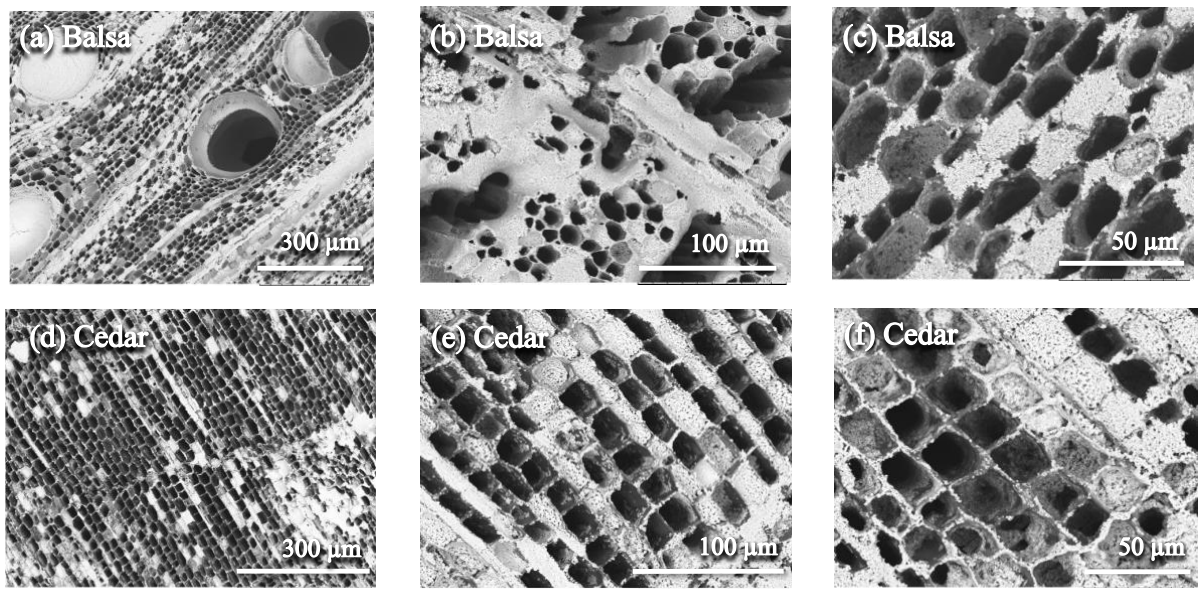

Figure 4.7: Atmospheric infiltrated (a – c) balsa template (d – f) cedar template, using the slurry with 10 wt% binder.

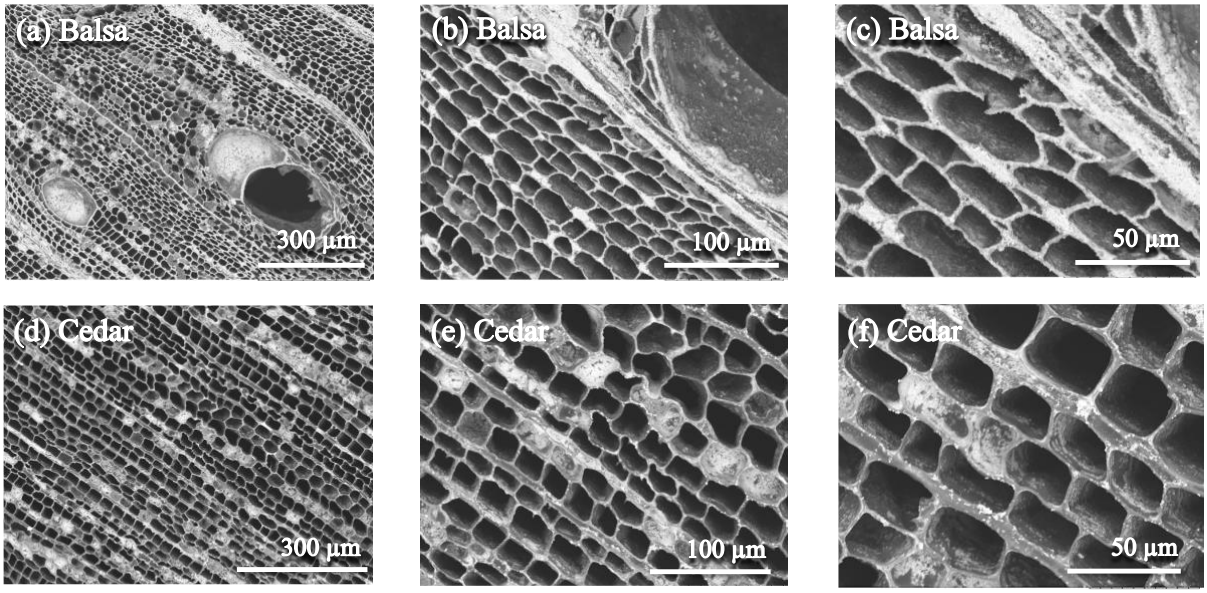

Figure 4.8: Vacuum infiltrated (a – c) balsa template (d – f) cedar template, using the slurry with 10 wt% binder.

In one hand, in the atmospheric infiltrated balsa, most of the pores in the balsa template were filled up with NZSP and characterized by closed pores as illustrated in Figure 4.7 (a – c). On the other hand, from the Figure 4.7 (d), numerous open pores were observed in the atmospheric infiltrated cedar template. However, almost all the pores in vacuum infiltrated balsa and cedar template stayed open (see Figure 4.8 (a – f)). A thin layer of homogeneous deposition of the

NZSP was observed in the pore walls of the balsa template infiltrated in vacuum (Figure 4.8(c)). In comparison to vacuum infiltrated balsa, the deposition of NZSP was not homogeneous on the pore walls of the vacuum infiltrated cedar (Figure 4.8 (f)).

4.3 Sintering studies of NZSP ceramic

Sintering of the infiltrated carbon template is an oxidation process in which the carbon template completely oxidizes leaving only the porous structure of the NZSP ceramic. The heating rate and sintering temperature was adopted and adjusted from the studies performed for sintering of NZSP (ref.[36]). As already mentioned, a slow heating rate of 3 °C/min was applied till 800 °C and then, after an intermediate dwelling of 2 h, the samples were heated at a rate of 5 °C/min until 1250 °C and set to dwell for 4 h. The intermediate dwelling step was performed to ensure the complete combustion of the carbon templates and organics (PVB). In this section, the sintered samples are analyzed, and their morphological, thermal, and dimensional change is reported in detail. In addition, a comparison between single and cyclic infiltration is also presented for both balsa and cedar wood.

4.3.1 Analysis of sintered ceramic based on infiltration method

The effect of infiltration methods (atmospheric and vacuum) on the structure of sintered NZSP ceramic is presented in this section. The Figures 4.9 illustrates the SEM images of NZSP ceramic after sintering both type of carbon templates infiltrated in atmospheric conditions. The microstructural morphology of balsa-derived NZSP ceramic is characterized mostly by blocked pore openings despite some open pores, (see Figure 4.9 (a – c)). This result is coherent with the observation made on the infiltrated balsa template shown in Figure 4.7 (a – c). However, dense solid columns were observed in cedar template (Figure 4.9 (d – f)) which is not the desired columnar hollow structure. Although SEM images (Figure 4.8 (d – f)) of the infiltrated cedar carbon template show numerous empty pores alongside the blocked ones, the dense solid blocks were observed after sintering. The probable reason of empty-looking pores in the infiltrated cedar template (Figure 4.7 (d)) might be the drainage of the liquid ceramic slurry from the pore opening. This phenomenon might take place due to the larger pore diameter of the cedar template which results in lower capillary forces between the ceramic particles in the

bulk and the pore walls. In addition, fragmented structures (Figure 4.9 (d)) for cedar-derived NZSP ceramic are observed. In contrast, the balsa-derived ceramic stayed as a single piece. This type of structure is not the goal of this research and therefore, the infiltration by dropping the ceramic slurry on the carbon templates using syringe was discarded from the possible options.

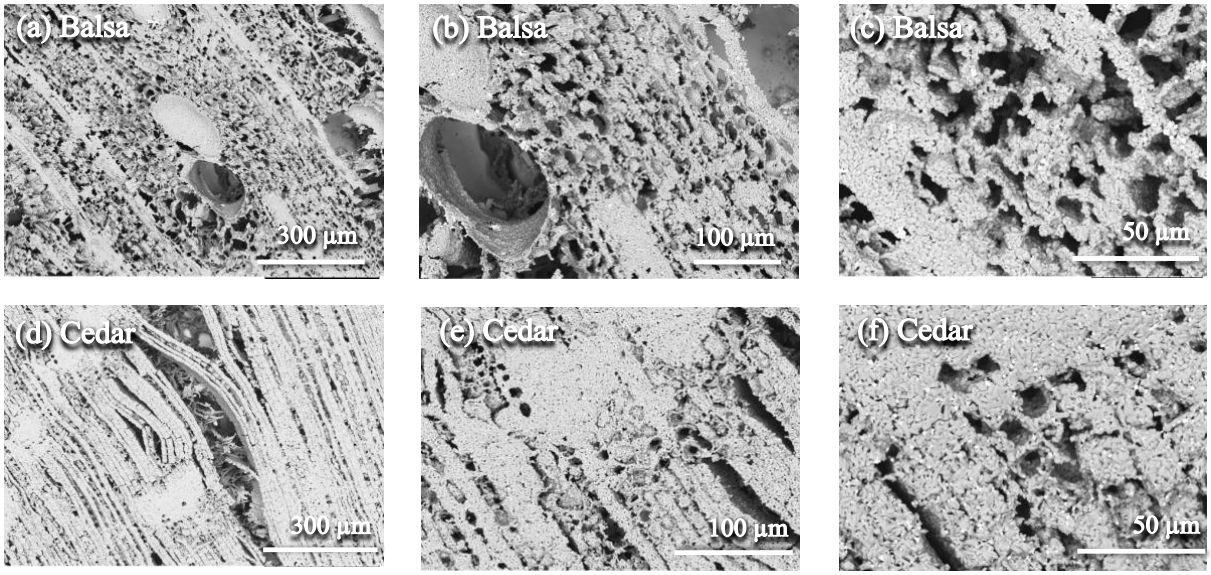

Figure 4.9: NZSP ceramic after sintering atmospheric infiltrated (a – c) balsa template, (d – f) cedar template. Infiltrated using the slurry with 10 wt% binder, and sintered at 1250 °C.

As a second option, vacuum infiltration was performed with the same slurry (10 wt% binder). It is worth noting that one single infiltration cycle was performed in this case. The microstructural images of NZSP ceramic after sintering the vacuum infiltrated balsa and cedar is presented in Figure 4.10.

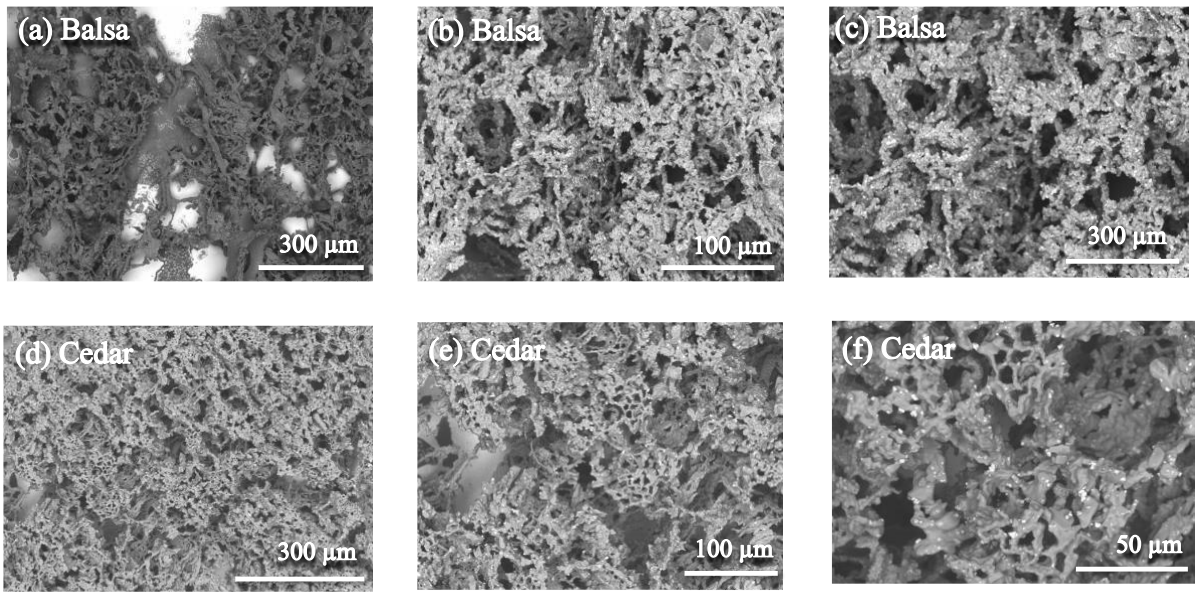

Figure 4.10: NZSP ceramic after sintering vacuum infiltrated (a – c) balsa template, (d – f) cedar template. Infiltrated using the slurry with 10 wt% binder, and sintered at 1250 °C.

For balsa, the structure appeared as an intertwined network of NZSP filaments (Figure 4.10 (a – c)) instead of taking the shape of balsa carbon template as desired. A similar pattern is also observed for cedar, however with micrometric level unidirectional porous structure formation scattered throughout the sample, Figure (4.10 (e)). This trace amount of structure formation shows the possibility of obtaining a unidirectionally oriented porous electrolyte replicating the wood microstructure. The intertwined network of NZSP formed in this phase of experiment can be referred to as a consequence of collapsing of the ceramic walls during the sintering step. The probable reason was deciphered as high binder content in the slurry which led to excess loading of binder and lower amount of NZSP ceramic within the carbon template. Although it appeared to be homogenous deposition of the NZSP ceramic on the balsa template, as illustrated in Figure 4.8 (b – c), the sintered ceramic collapsed due to less amount of NZSP ceramic. From this observation it is evident that slurry composition plays a crucial role in determining the structure of the sintered ceramic. With this realization, the binder content was reduced in the slurry and the carbon templates were infiltrated with the optimized slurry.

4.3.2 Ceramic with optimized slurry and cyclic infiltration

Because of the previously unsatisfying experiments, the slurry was modified by decreasing the binder content to 5 wt% with respect to the powder content. The overall solid content remained similar to the previously mentioned slurry composition (Table 3.1), i.e. 24.4 wt% (approximately). Vacuum infiltration was performed in this step. Moreover, the carbon templates were kept in the slurry for 30 min and allowed the slurry to be dried. For balsa, the thickness of the carbon template was 3 mm while it was 1 mm for the cedar template. The morphology of the resulting structures after sintering is presented in the Figure 4.11.

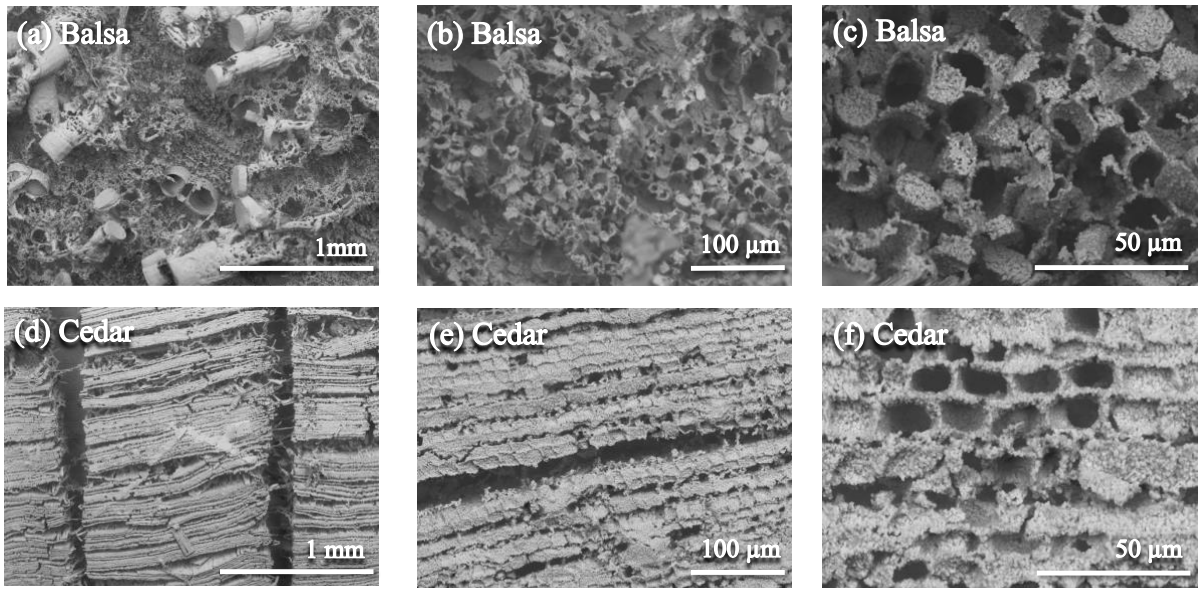

Figure 4.11: NZSP ceramic after sintering vacuum infiltrated (a – c) balsa template, (d – f) cedar template. The templates were kept in the slurry and infiltration was performed in vacuum until the slurry dried. Infiltrated using the slurry with 5 wt% binder and sintered at 1250 °C.

In this case, the microstructure of balsa-derived NZSP ceramic was characterized by collapsed tubular channels. The tubes formed of the large pores experienced the collapse in the bottom part and either fell down or tilted (Figure 4.11(a)). Similar patterns were observed for the medium-sized pores as well. This collapse can be interpreted as a consequence of increased thickness of the template (height of the columns) which induced extra weight on the structure. The thickness of the ceramic walls was simply not large enough to bear this extra load. Despite collapsing, tubular porous structures are formed, following the exact replica of the balsa template (Figure 4.11(c)). Moreover, the smooth surface and even thickness (Figure 4.11(a)

and (c)) of the formed ceramic walls ensures a homogenous deposition of the NZSP ceramic particles on the pore walls of the carbon template (balsa).

A completely opposite microstructural pattern was observed in the case of the cedar-derived NZSP ceramic. The pores were found to be completely filled with NZSP ceramic which ultimately resulted in dense solid blocks (Figure 4.11(d – f)) similar to the one observed with syringe filling. This phenomenon resulted from the drying of the slurry inside the pores. Therefore, this experiment shaded light on the necessity of draining the excess slurry from the bulk of the pores. In this way, only the ceramics attached to the pore walls will stay and the rest of the liquid will drain out of the pores. This draining of the excess slurry promises the possibility of forming the desired columnar hollow structure.

In the second approach with this slurry composition (5 wt% binder), the templates were completely soaked in the slurry and kept in it for 10 min. After this first infiltration, the samples were put in Petri dish and allowed to drain out the excess slurry from the bulk of the channels. The infiltrated templates were then dried in vacuum for 30 min before they were infiltrated again. A similar draining process was followed in the second cycle as well. The sintered ceramics obtained by infiltrating the carbon templates twice are presented in Figure 4.12.

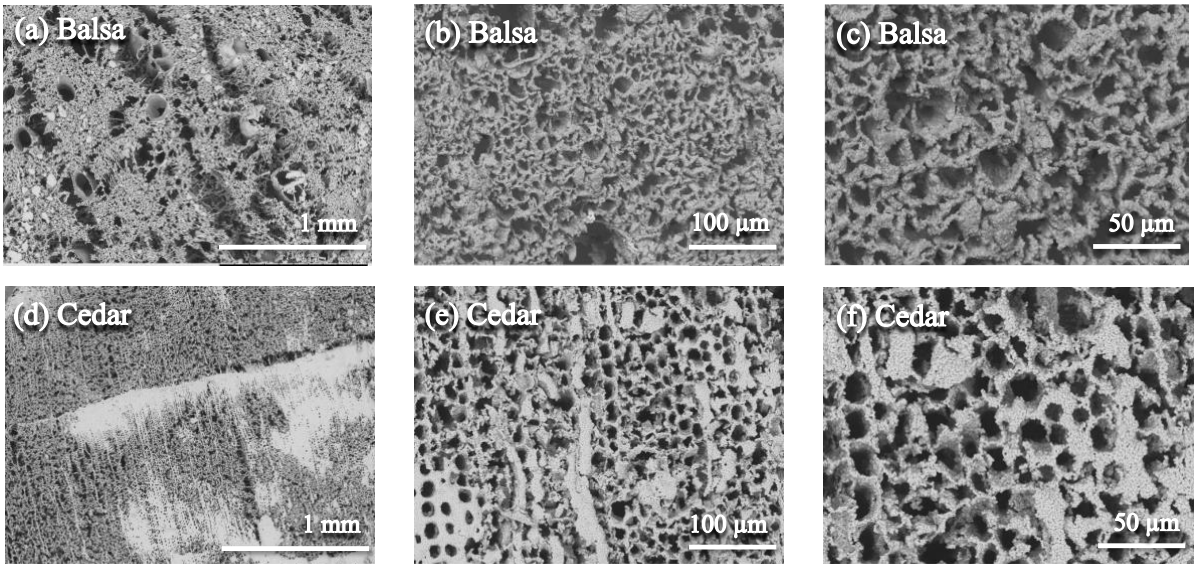

Figure 4.12: Sintered ceramics after two infiltrations using the slurry with 5 wt% binder, (a – c) infiltrated balsa template, (d – f) cedar template.

First of all, unlike the previously mentioned result shown in Figure 4.11 (a and d), no collapse or fragmentation was observed. Instead, sintered samples retained in one piece. The combined action of reducing the binder content in the slurry and cyclic infiltration ensured adequate amount of powder deposition in the pore walls. The images in Figure 4.12 (c and f) shows that the intended hollow columnar ceramic structures were formed for the first time with exact replica of both types of carbon templates. These hollow columnar structures are facilitated by the draining of the excess ceramic slurry from the bulk of the microchannels. A total void fraction of 40.6 vol% and 43.8 vol% were calculated for balsa- and cedar-driven ceramics, respectively. The average pore diameters were 5 – 10 μm and 10 – 15 μm for balsa and cedar, respectively. Importantly, the average wall thickness for both balsa- and cedar-assisted ceramic structures is found to be 6 – 10 μm. This information is useful as it provides insight on the ceramic wall thickness required to prevent the structure from collapsing. These sintered ceramic samples were examined further to detect any interconnection between the porous channels. No interconnecting small pores, similar to the ones on the walls of pyrolyzed cedar template as illustrated in the Figures 4.3 (f) were observed. In case of balsa, these pores were absent the from pyrolyzed carbon template. Although the expected interconnection between the channels were not generated, the channels are still well connected. These interconnections between the channels are mainly generated by the cracks, the inhomogeneous deposition of the ceramic on the carbon template walls, and the collapse of the ceramic walls. Therefore, it can be claimed that unidirectional and interconnected porous channels have been fabricated successfully to meet the requirements necessary for application as an electrolyte scaffold.

The XRD analysis was performed for both balsa- and cedar-derived ceramic structures and is presented in the Figure 4.13 below.

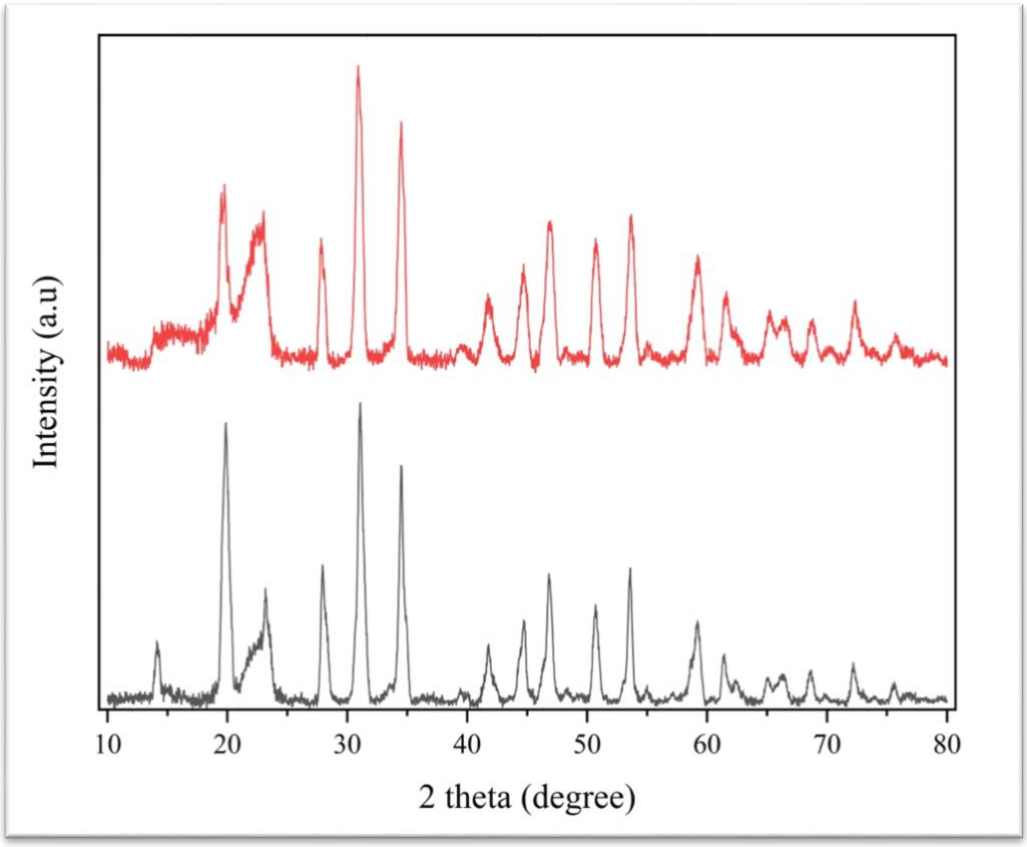

Figure 4.13: XRD analysis of sintered NZSP ceramic. Red: cedar-derived NZSP ceramic, black: balsa-derived NZSP ceramic. x-axis: intensity (a.u), y-axis: 2 theta (degree).

The XRD pattern of both the balsa- and cedar-derived ceramic was matched against ICDD reference data (reference code: 01-078-2347) and NASICON phase with rhombohedral (R$\underline{3}$c) crystal system was confirmed.

4.3.3 Thermal studies of the sintered ceramic

The thermal studies of the sintered porous NZSP ceramic mainly focuses on the dimensional changes and bending of the sintered ceramic. Since the drying of raw wood to sintering of the ceramic, the prepared NZSP ceramics shrank by approximately 40% in the axial direction and 50% along the radius in total. These values are closely identical for both balsa and cedar as templates. Overall, 85% of volume shrinkage was observed. Apart from this, analysis of the bending formation is crucial for preventing the structure from falling apart.

The bending mechanism for the ceramic during sintering process is similar to that of wood during pyrolysis, as illustrated in Figure 4.4 (a). Detailed explanations were published by Hasegawa and Hayashi, (2023) (ref.[10]). In short, the ceramic pellets experience high shear force due to sintering. Due to varying densities across the pellet, they experience varying shrinkage which causes bending of the ceramic layers. This higher degree of bending ultimately induce cracks causing the structure fall apart. This mechanism is common for both the dense and the porous electrolytes. In the case of the dense layers, adding an extra weight would minimize the degree of bending and cracking. However, this technique is not feasible for the porous layer as the weight will distort the microstructure. It is worth noting that the NZSP ceramic starts to form NASICON phase at around 1200 °C while the carbon template completely oxidizes at around 800 °C. In addition, NZSP remains powder even at the temperature of 900 °C. The additional weight would exert force on the ceramic structure still being under powder form which would cause collapse of the structure. Due to closed pore openings in the carbon templates originating from the cutting process and inhomogeneous infiltration of the template by the ceramics, the density of the ceramic throughout the sample varies. Therefore, ensuring homogeneous infiltration of the templates by the ceramics is essential. This challenge could be solved by ensuring undamaged pore openings and further optimizing the slurry composition.

5 EIT chapter

5.1 Life cycle and circular economy

In this research, a porous NASICON-type NZSP electrolyte structure was aimed which has similar life cycle as of other conventional solid-state electrolytes. The life cycle starts with mining the materials, for instance Na, Zr, Si, and P, and follows the steps of precursor reagents production, electrolyte synthesis, thermal treatment, battery manufacturing, use, recycling or disposal. This product is a versatile structure that promises immense potential to the circular economy through the use of cheaper and noncritical raw materials. Although the development is in the research stage, similar analysis by Yi et al. (2020) showed that with these porous electrolyte architectures batteries can provide 1.8 to 2.2 times higher energy density compared to the conventional electrolytes[22]. By significantly enhancing the performance with minimum amount of materials possible, this product directly supports the circular economy's fundamental principles of reducing waste generation, promoting resource efficiency and ensuring sustainable supply of raw materials for future generation[37]. The life cycle of batteries is presented in Figure 5.1.

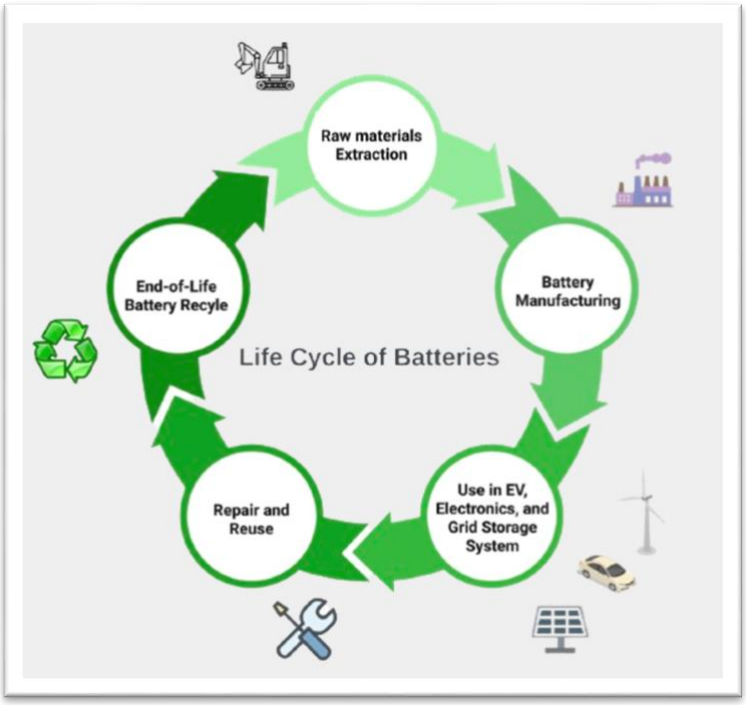

Figure 5.1: Life cycle of conventional batteries.

The scope for performing a life cycle analysis (LCA) of this product is broad and should be analyzed at a higher technology readiness level. The foremost challenge is imposed by limited data on the manufacturing process and end of life management. Moreover, it depends on the type of active materials used to prepare the battery. The electrolyte itself cannot decide on the overall outcome although it does not contain any toxic material like vanadium, cobalt or chromium. The overall outcome would depend on the other components (anode, cathode, etc.) of the battery as well. Despite limitations, a full-scale life cycle analysis will illustrate its comprehensive impact on the environment, compare between technologies, and foster the decision-making process about sustainable improvement.

Although LCA has not been performed due to lack of data, it can be commented based on the considerations, for instance raw materials extraction, transport, battery manufacturing, and end of life management[38]. The main sources of impact will result from raw materials extraction (Na, Zr, Si, and P), precursor synthesis, sintering, and end of life processing steps. The raw materials mining (except Na) requires energy intensive processes, for instance operating the equipment, mineral processing, and transportation that are powered by burning fuel. This leads to greenhouse gas emission that causes global warming. Moreover, the chemicals used during the extraction process impose significant threat of toxicity and ecotoxicity. The increase of this impact category is also caused by the precursor synthesis step. In addition, mining uses significant amount of water and land, causing potential threat to biodiversity and habitat. The sintering process during manufacturing requires high amount of thermal energy. The energy production process along with the gases formed from the oxidation of carbon template emits gases, such as CO_2, SO_2, CO, and etc. that might cause acidification. However, this contribution is negligible as compared to the aforementioned step. The NZSP electrolyte contains phosphate groups that might cause eutrophication (both marine and fresh water) if not treated properly at the end of life.

This type of electrolyte structure can be formed with other kind of ceramic as well. By choosing NZSP as the target materials, we avoided the risk factor originating from the procurement of critical materials. Therefore, the raw materials availability will be higher. In addition, the critical materials will be reserved for future, strengthening the future supply of raw materials. All of the elements (Na, Zr, Si, P) used in developing this product are abundant in the Earth's crust. The concentration of sodium, zirconium, silicon, and phosphorus are 23600 ppm, 132 ppm, 282000 ppm and 567 ppm, respectively. Therefore, due to their abundance, NZSP

production is at low risk globally[19]. However, similar to 2020, phosphorous is included in the critical raw materials list 2023 by the European Union although it is not in the strategic raw materials[39]. The possibility of phosphorus to be included in the critical materials list is high due to the monopoly of China, which supplies the world's 79% phosphorous and 48% phosphate salt[39]. Assuming that NZSP will be implemented at first in the European Union, originating from Germany. The European Union determines the criticality of any material based on its economic importance and potential supply risk to Europe[39]. In 2022, Germany was the 3rd largest importer of phosphorus, with imports totaling M$144. They sourced phosphorus from countries such as Kazakhstan, Poland, Italy, and Vietnam[40]. This diversification suggests that China's dominance in phosphorus supply is unlikely to disrupt the Germany's supply chain in the future.

5.2 Techno-economic Analysis

5.2.1 Technological analysis

The technology to manufacture porous NZSP electrolyte using templating method is similar to other conventional methods including freeze tape casting and using pore formers. The full process includes raw materials acquisition, precursor preparation, NZSP synthesis, slurry preparation, electrolyte fabrication, and sintering. In this research, the porous scaffold was synthesized at first and then planned to attach it to the dense layer before sintering. The dense layer will be made of the same NZSP ceramic through conventional tape-casting process. For other techniques such as freeze tape casting, the porous and dense layer is fabricated at the same time. Here, the porous layer is prepared first and then attached to the dense layer, increasing one additional step. It is expected to obtain considerably higher amount of output to compensate this additional step. However, comments can only be made after obtaining all the test results on the performance and defining the standard process for the industries. The goal is to obtain energy density as high as 200 Wh kg^{-1}.

5.2.2 Economic Analysis

The business policy depends on the performance of the batteries made out of this type of electrolyte structure. If the newly designed product is successful in enhancing the performance of the solid-state-batteries, there is a huge potential market throughout the world. Various markets, for instance electric vehicles (EV), portable electronics, wearables, power tools, stationary power supply, aeronautics will benefit from this product. The global market value of the battery sector was B$112 in 2021; it is currently growing at a rate of 16.68% and is expected to reach a market of B$424 by 2030 (ref.[41]). Therefore, it is obvious that more batteries will be manufactured in the future and there is a potential of innovative business opportunity.

Either the electrolyte itself or the full cell (battery) offers the value proposition of offering high performance, safety, longevity, and reduced materials criticality. Different types of business strategies, for instance B2B, and B2C, are possible with this product. In the B2B business model, bulk quantity of the products will be sold to the industries, including grid storage systems, EV, and consumer electronics manufacturers, while the individual customers are the main segment in the B2C model. The first model is preferred and is planned to distribute the products directly by engaging the large manufacturers of EV, and electronics through networking during trade shows and conferences. Possible consumer companies include Tesla INC, BMW group, Volkswagen group, Samsung electronics, Apple Inc, Siemens AG and etc. Specialized distributors will also be engaged to supply products to smaller manufacturers and relatively small markets. The customers will be supported through strategic partnerships, technical support, and incentive programs for maintaining co-developments and long-term supply agreements. In return, the revenue collection is planned from the product sales, licensing, consultancy, and research projects from government and private agencies. Highly skilled group of marketing and R&D teams are required to maintain the product development, quality, marketing, and supply chain management. In addition, ensuring manufacturing facilities and raw materials supply chain is also essential. We will create partnership with the materials suppliers, manufacturing farms, academics, and stakeholders who influence the regulations and standards. Companies including BASF (Na), Merck KGaA (Na), Zircomet (Zr), Silitronic AG (Si), Sasol Germany GmbH (P) are potential raw materials and chemical reagents suppliers and manufacturing partners. In addition, the European Commission, European Chemicals Agency (ECHA), German Environment Agency (UBA), and

Environmental Action Germany (DUH) are the potential regulatory and environmental protection-related stakeholders. The main expenditure will be in research and development, manufacturing, marketing, and running the administration. The overall business model canvas is illustrated in following Table 5.1:

Table 5.1: Business model canvas for porous solid-state electrolyte.

<table>
<tr><th>Key Partners</th><th>Key Activities</th><th>Value Propositions</th><th>Customer Relationships</th><th>Customer segments</th></tr>
<tr><td rowspan="3">Materials Suppliers, Manufacturing Partners, Academics and Research Institutes, Distributors, Consumer Industry Groups, Environmental and Regulatory Stakeholders, Business Angels</td><td>Research and Product Development, Quality Control, Marketing and Sales, Supply Chain Management of Raw Materials</td><td rowspan="3">High Performance, Safety, Longevity, Reduced Materials Criticality</td><td>Strategic Partnership, Technical and Consultancy Support, Incentives for Long Term Customers</td><td rowspan="3">Electric Vehicles (EV) and Consumer Electronics Manufacturer, Grid Scale Energy Storage Systems, R&D Institutions</td></tr>
<tr><td>Key Resources</td><td>Channels</td></tr>
<tr><td>Human Resources (Marketing, Research, and Administration)</td><td>Direct Sale, Distributors, Trade Shows and Conferences</td></tr>
<tr><td colspan="2">Cost Structure</td><td colspan="3">Revenue Streams</td></tr>
<tr><td colspan="2">R&D Expenses, Manufacturing Costs, Marketing and Sales, Operational Costs</td><td colspan="3">Selling Porous Electrolyte, Licensing the Technology, Research Funds</td></tr>
</table>

5.3 SWOT analysis

Strength, Weakness, Opportunity, and Threat (SWOT) analysis is a useful technique to assess the company's present situation and decide the strategic planning. Similarly, advantages and challenges of the electrolyte business was analyzed and is presented in Table 5.2.

Table 5.2: SWOT analysis of porous solid-state electrolyte.

SWOT Analysis	
Strength	**Weakness**
Innovative Approach, Resource Efficiency, High Performance, Safety, Longevity, Reduced Materials Criticality, Positive Social and Environmental Impact	Scalability, Data Requirement, Initial Cost
Opportunities	**Threats**
Market Demand, Partnership, Government Initiatives	Competitors, Market Volatility, Regulatory Changes

5.3.1 Strength

The innovative approach designed simple process steps to develop electrolyte with high performance, energy efficiency, safety and longevity utilizing minimum amounts of critical materials. Consequently, it will put positive impact both to the society and environment through maintaining the circular economy model. The product is a strong competitor in the market due to its suitability for wide range of applications and enhanced safety.

5.3.2 Weakness

The main weakness of the product is its scalability. As the process is not fully developed yet, the challenges in scaling up the production while maintaining the consistent quality and cost efficiency could not be analyzed. However, the process itself is not complicated, so scaling up should be possible. With further acquisition of relevant experimental data and equipment, potential barriers to large scale production can be overcome. Apart from this, the collection of

initial capital and high initial cost to set up the manufacturing plant, hire staffs, and operate logistics could severely hinder the implementation of this innovative product in the market.

5.3.3 Opportunities

The product is well-promising to capitalize on the growing market demand for sustainable energy storage systems. It can attract clients seeking to improve their product's safety, longevity, performance, and environmental footprint by offering innovative solutions. Furthermore, forming strategic partnerships with technology providers, equipment manufacturers, and sustainability consultants can enhance the product's service offerings and create new business opportunities. The business theme also aligns with government initiatives of promoting sustainable greener energy production and storage. This allows to access potential funding and gain recognition in the market.

5.3.4 Strength

The potential threat comes from the companies offering similar products and services. The fluctuations in raw materials price, although minimum, can impact the willingness of potential clients to invest, making market volatility a concern. Another reason for market volatility might origin from the lower price of our product, as it is made of relatively cheap and abundant materials. Additionally, changes in environmental regulations can affect the mining industries extracting the required minerals, potentially affecting the supply chain. It is crucial to navigate these threats while leveraging the project's strengths and opportunities to succeed in the market.

6 Conclusion and future direction

6.1 Conclusion

Fixing a lot of experimental parameters, for instance template preparation, slurry composition, infiltration conditions is a challenge imposed by the templating method. However, once these parameters are set, process of replicating the wood microstructure is a simple and easy process that requires low energy input. In addition, the wood microstructure templating method showed the feasibility of obtaining a structure with unidirectionally oriented pores which is not a easily done with other techniques. Two different wood templates, i.e. balsa and cedar, yielded microstructures with different pore diameters: 5 – 10 µm and 10 – 15 µm, respectively. Pore wall thicknesses of 6 – 10 µm were observed. This illustrates the possibility of obtaining microstructures with different pore diameters according to the intended goal. Overall, the development of a porous ceramic electrolyte scaffold with NZSP was successfully realized. For the intended battery application, the above-mentioned microstructures are desired as they will offer a scaffold with very low tortuosity.

Apart from this positive experimental outcome, the product will follow the same life cycle as of other conventional solid-state batteries. Unlike others, this electrolyte is made of cheaper materials and is free of toxic and critical materials, which offers closer alignment with that of circular economy through promoting resource efficiency and sustainability. Moreover, this product offers promising business potential for the growing battery market because of its high performance, longevity, and safety.

6.2 Future direction

The solid electrolytes perform the function of a separator in addition to an ion-conducting membrane. Till now, the porous scaffold of the electrolyte has been synthesized, which will accommodate the cathode materials. However, the cathode materials will pass through the pores of the scaffold and make contact with the anode materials, which will cause short circuit. A dense layer (similar to the solid electrolyte in Figure 1.1(b) marked by orange circle) made of the same NZSP ceramic (without any pore) would serve the function of the separator and prevent the contact between the electrode materials. Therefore, it needs to be attached on one

side of the porous scaffold. The idea to form a double layer is to glue the tape-cast layer and infiltrated carbon template (before sintering) with NZSP slurry and then sinter them together. The porous scaffold preparation has been explained throughout this manuscript. The conventional technique for preparing the dense solid-state electrolyte is tape casting[10]. The tape casting requires slurry preparation which includes the NZSP ceramic powder, solvent, and other additives like binder and dispersants. After the slurry is prepared, it is casted using the doctor blade to prepare the tapes according to desired thickness. After drying the cast tapes, they can be cut in the desired dimensions. At this point the infiltrated carbon template will be glued on the tape with NZSP slurry and will be sintered together. If this step is successful, the investigation will continue with the infiltration of active materials into the porous scaffold of the bi-layer electrolyte and assembly of a battery cell. A schematic process flow diagram is presented in Figure 6.1 illustrating the idea on synthesizing a bilayer electrolyte.

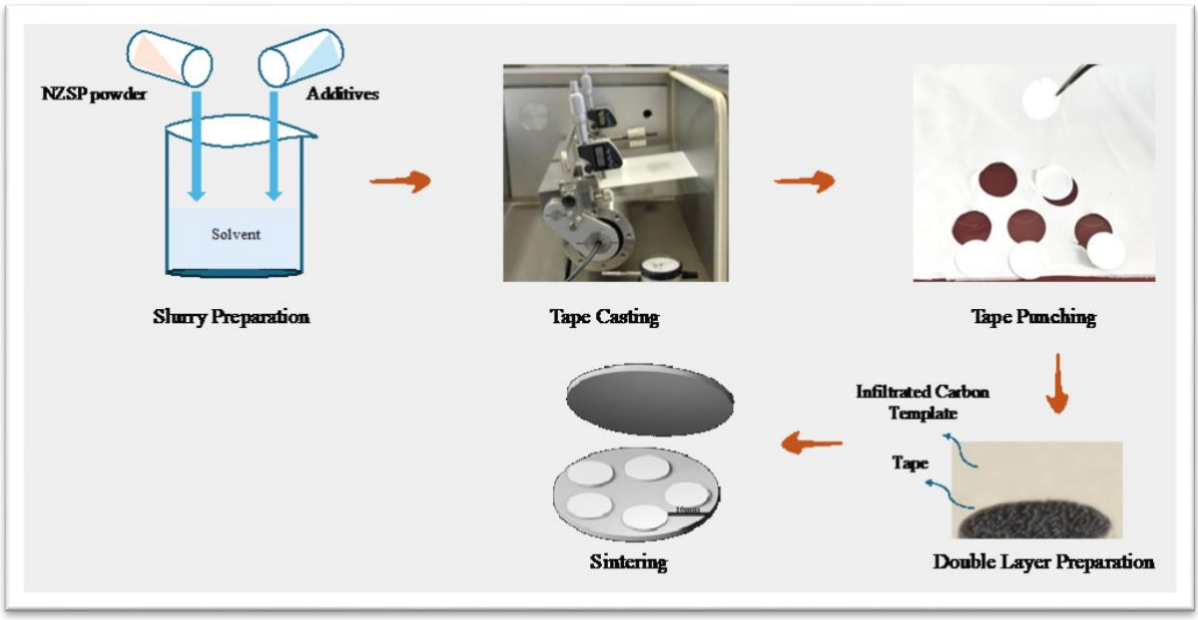

Figure 6.1: Schematic diagram for bilayer electrolyte preparation.

Acknowledgement

I express my heartfelt gratitude to the Forschungszentrum Jülich GmbH, University of Liège, and AMIR EMJM consortium for arranging and supporting my master's thesis academically and financially. I am deeply indebted to Dr. Frank Tietz, Prof. Nathalie Job, and Prof. Grégoire Léonard for their cordial effort in solving the administrative issues and supervising me till the completion of this research. In addition, I express my sincere gratitude to Dr. Monika Bhardwaj, Dr. Enkhtsetseg Dashjav, and Mrs. Marie-Thères Gerhards for their guidance and mentorship as my co-supervisors. Their expertise and guidance have added invaluable enrichment to my research experience. I would also like to thank Mr. Volker Bader for his cordial helping hand in preparing the carbon templates and sintering the porous ceramics. Last, but not the least, I would like to thank all my friends and mentors, especially Prof. Guido Sonnemann from the AMIR master program for hosting such an enriching journey throughout this program.

7 References

1. Abraham, K. M. How Comparable Are Sodium-Ion Batteries to Lithium-Ion Counterparts? *ACS Energy Letters* **5**, 3544–3547 (2020).
2. Abraham, K. M. Prospects and limits of energy storage in batteries. *Journal of Physical Chemistry Letters* vol. 6 830–844 (2015).
3. Hu, C. Nanotechnology based on anode and cathode materials of sodium-ion battery. *Applied and Computational Engineering* **26**, 164–171 (2023).
4. Massaro, A., Pecoraro, A., Muñoz-García, A. B. & Pavone, M. First-Principles Study of Na Intercalation and Diffusion Mechanisms at 2D MoS_2/Graphene Interfaces. *Journal of Physical Chemistry C* **125**, 2276–2286 (2021).
5. Wang, L. P., Yu, L., Srinivasan, M., Xu, Z. J. & Wang, X. Recent developments in electrode materials for sodium-ion batteries. *Journal of Materials Chemistry A* vol. 3 9353–9378 (2015).
6. Lu, W., Wang, Z. & Zhong, S. Sodium-ion battery technology: Advanced anodes, cathodes and electrolytes. *J. Phys.: Conf. Ser.* **2109**, 012004 (2021).
7. Janek, J. & Zeier, W. G. A solid future for battery development. *Nat Energy* **1**, 16141 (2016).
8. Yang, Z., Tang, B., Xie, Z. & Zhou, Z. NASICON-Type $Na_3Zr_2Si_2PO_{12}$ Solid-State Electrolytes for Sodium Batteries**. *ChemElectroChem* **8**, 1035–1047 (2021).
9. Yang, H.-L. *et al.* Progress and Challenges for All-Solid-State Sodium Batteries. *Adv Energy and Sustain Res* **2**, 2000057 (2021).
10. Hasegawa, G. & Hayashi, K. NASICON-based all-solid-state Na–ion batteries: A perspective on manufacturing via tape-casting process. *APL Energy* **1**, 020902 (2023).
11. Goodenough, J. B., Hong, H. Y.-P. & Kafalas, J. A. Fast Na^+-ion transport in skeleton structures. *Materials Research Bulletin* **11**, 203–220 (1976).

12. Naqash, S., Tietz, F., Yazhenskikh, E., Müller, M. & Guillon, O. Impact of sodium excess on electrical conductivity of $Na_3Zr_2Si_2PO_{12}$ + xNa_2O ceramics. *Solid State Ionics* **336**, 57–66 (2019).
13. Zhao, C. *et al.* Solid-State Sodium Batteries. *Advanced Energy Materials* **8**, 1703012 (2018).
14. Ma, Q. *et al.* Scandium-Substituted $Na_3Zr_2(SiO_4)_2(PO_4)$ Prepared by a Solution-Assisted Solid-State Reaction Method as Sodium-Ion Conductors. *Chem. Mater.* **28**, 4821–4828 (2016).
15. Ma, Q. & Tietz, F. Solid-State Electrolyte Materials for Sodium Batteries: Towards Practical Applications. *ChemElectroChem* vol. 7 2693–2713 (2020).
16. Kiritharan, S. *et al.* Porosity characterisation of solid-state battery electrolyte with terahertz time-domain spectroscopy. *Journal of Power Sources* **595**, 234050 (2024).
17. Kotobuki, M. *et al.* A novel structure of ceramics electrolyte for future lithium battery. *Journal of Power Sources* **196**, 9815–9819 (2011).
18. Zhao, Q., Stalin, S., Zhao, C. Z. & Archer, L. A. Designing solid-state electrolytes for safe, energy-dense batteries. *Nature Reviews Materials* vol. 5 229–252 (2020).
19. Jaschin, P. W., Tang, C. R. & Wachsman, E. D. High-rate cycling in 3D dual-doped NASICON architectures toward room-temperature sodium-metal-anode solid-state batteries. *Energy Environ. Sci.* **17**, 727–737 (2024).
20. Zhang, H. *et al.* Garnet-Based Solid-State Li Batteries with High-Surface-Area Porous LLZO Membranes. *ACS Applied Materials and Interfaces* **16**, 12353–12362 (2024).
21. Shen, H. *et al.* Scalable Freeze-Tape-Casting Fabrication and Pore Structure Analysis of 3D LLZO Solid-State Electrolytes. *ACS Applied Materials and Interfaces* **12**, 3494–3501 (2020).

22. Yi, E. *et al.* All-Solid-State Batteries Using Rationally Designed Garnet Electrolyte Frameworks. *ACS Applied Energy Materials* **3**, 170–175 (2020).
23. Okada, K. *et al.* Porous ceramics mimicking nature—preparation and properties of microstructures with unidirectionally oriented pores. *Science and Technology of Advanced Materials* **12**, 064701 (2011).
24. Cao, J., Rambo, C. R. & Sieber, H. Preparation of Porous Al_2O_3-Ceramics by Biotemplating of Wood. *Journal of Porous Materials* vol. 11 163–172 (2004).
25. Vogli, E., Sieber, H. & Greil, P. Biomorphic SiC-ceramic prepared by Si-vapor phase infiltration of wood. *Journal of the European Ceramic Society* **22**, 2663–2668 (2002).
26. Novais, R. M. & Pullar, R. C. Comparison of low and high pressure infiltration regimes on the density and highly porous microstructure of ceria ecoceramics made from sustainable cork templates. *Journal of the European Ceramic Society* **39**, 1287–1296 (2019).
27. Persembe, E., Parra-Cabrera, C. & Ameloot, R. Ceramic Foams with Controlled Geometries Through 3D-Printed Sacrificial Templates. *Advanced Engineering Materials* **25**, 2300076 (2023).
28. Greil, P. Biomorphous Ceramics From Lignocellulosics. *Journal of the European Ceramic Society* **21**, 105–118 (2001).
29. Sieber, H., Hoffmann, C., Kaindl, A. & Greil, P. Biomorphic cellular ceramics. *Advanced Engineering Materials* **2**, 105–109 (2000).
30. Jing, W. *et al.* Pore structure engineering of wood-derived hard carbon enables their high-capacity and cycle-stable sodium storage properties. *Electrochimica Acta* **391**, 139000 (2021).
31. Gao, X. *et al.* Wood-inspired high-performing hierarchical porous $Ce_{0.7}Zr_{0.3}O_2$ catalyst for low-temperature selective catalytic reduction of NO_x by NH_3. *Ceramics International* **47**, 29149–29161 (2021).

32. Kumar, A., Jyske, T. & Petrič, M. Delignified Wood from Understanding the Hierarchically Aligned Cellulosic Structures to Creating Novel Functional Materials: A Review. *Advanced Sustainable Systems* **5**, 2000251 (2021).
33. Bataillou, G. *et al.* Cedar Wood-Based Biochar: Properties, Characterization, and Applications as Anodes in Microbial Fuel Cell. *Applied Biochemistry and Biotechnology* **194**, 4169–4186 (2022).
34. Shishkina, O., Lomov, S. V., Verpoest, I. & Gorbatikh, L. Structure-property relations for balsa wood as a function of density: Modelling approach. *Archive of Applied Mechanics* **84**, 789–805 (2014).
35. Elustondo, D., Matan, N., Langrish, T. & Pang, S. Advances in wood drying research and development. *Drying Technology* **41**, 890–914 (2023).
36. Naqash, S., Sebold, D., Tietz, F. & Guillon, O. Microstructure–conductivity relationship of $Na_3Zr_2(SiO_4)_2(PO_4)$ ceramics. *Journal of the American Ceramic Society* **102**, 1057–1070 (2019).
37. Moraga, G. *et al.* Circular economy indicators: What do they measure? *Resources, Conservation and Recycling* **146**, 452–461 (2019).
38. Porzio, J. & Scown, C. D. Life-Cycle Assessment Considerations for Batteries and Battery Materials. *Advanced Energy Materials* **11**, 2100771 (2021).
39. European Commission. Directorate General for Internal Market, Industry, Entrepreneurship and SMEs. *Study on the Critical Raw Materials for the EU 2023: Final Report.* (Publications Office, LU, 2023).
40. OEC. *Phosphorus in Germany*. https://oec.world/en/profile/bilateral-product/phosphorus/reporter/deu. Page accessed on June 8, 2024.
41. Melissa, R. *Global Battery Market Keeps Expanding to Reach USD 424 Billion by 2030*. https://statzon.com/insights/global-battery-market. Page accessed on June 8, 2024.